Integrated light chemical tagging analyses of seven M31 outer halo globular clusters from the Pan-Andromeda Archaeological Survey

Monthly Notices of the ROYAL ASTRONOMICAL SOCIETY

MNRAS **448,** 1314–1334 (2015) doi:10.1093/mnras/stv020

Integrated light chemical tagging analyses of seven M31 outer halo globular clusters from the Pan-Andromeda Archaeological Survey⋆

Charli M. Sakari,[1]†‡§ Kim A. Venn,[1] Dougal Mackey,[2] Matthew D. Shetrone,[3] Aaron Dotter,[2] Annette M. N. Ferguson[4] and Avon Huxor[5]

[1]*Department of Physics and Astronomy, University of Victoria, Victoria, BC V8W 3P2, Canada*
[2]*Research School of Astronomy and Astrophysics, The Australian National University, Weston, ACT 2611, Australia*
[3]*McDonald Observatory, University of Texas at Austin, HC75 Box 1337-MCD, Fort Davis, TX 79734, USA*
[4]*Institute for Astronomy, University of Edinburgh, Royal Observatory, Blackford Hill, Edinburgh EH9 3HJ, UK*
[5]*Astronomisches Rechen-Institut, Universität Heidelberg, Mönchhofstraße 12-14, D-69120 Heidelberg, Germany*

Accepted 2015 January 3. Received 2014 December 23; in original form 2014 November 24

ABSTRACT

Detailed chemical abundances are presented for seven M31 outer halo globular clusters (with projected distances from M31 greater than 30 kpc), as derived from high-resolution integrated light spectra taken with the Hobby–Eberly Telescope. Five of these clusters were recently discovered in the Pan-Andromeda Archaeological Survey (PAndAS) – this paper presents the first determinations of integrated Fe, Na, Mg, Ca, Ti, Ni, Ba, and Eu abundances for these clusters. Four of the target clusters (PA06, PA53, PA54, and PA56) are metal poor ([Fe/H] < -1.5), α-enhanced (though they are possibly less α-enhanced than Milky Way stars at the 1σ level), and show signs of star-to-star Na and Mg variations. The other three globular clusters (H10, H23, and PA17) are more metal rich, with metallicities ranging from [Fe/H] $= -1.4$ to -0.9. While H23 is chemically similar to Milky Way field stars, Milky Way globular clusters, and other M31 clusters, H10 and PA17, have moderately low [Ca/Fe], compared to Milky Way field stars and clusters. Additionally, PA17's high [Mg/Ca] and [Ba/Eu] ratios are distinct from Milky Way stars, and are in better agreement with the stars and clusters in the Large Magellanic Cloud. None of the clusters studied here can be conclusively linked to any of the identified streams from PAndAS; however, based on their locations, kinematics, metallicities, and detailed abundances, the most metal-rich PAndAS clusters H23 and PA17 may be associated with the progenitor of the Giant Stellar Stream, H10 may be associated with the SW cloud, and PA53 and PA56 may be associated with the eastern cloud.

Key words: globular clusters: general – galaxies: abundances – galaxies: evolution – galaxies: individual: M31 – galaxies: star clusters: general.

1 INTRODUCTION

The Andromeda galaxy (M31) is the nearest large neighbour to the Milky Way (MW). Its relative proximity offers a unique opportunity to study the stellar populations of a nearby, large galaxy without being hindered by interstellar extinction. Though the stars in M31 are considerably fainter than MW field stars, they can still be resolved for photometric and low-resolution spectroscopic observations while entire globular clusters (GCs) can be targeted for integrated light (IL) spectroscopy. Such observations contribute to studies of the formation and evolution of M31 and its satellite system.

Deep surveys of M31's outer regions, such as the Isaac Newton Telescope (INT) survey (Ibata et al. 2001; Ferguson et al. 2002) and the Pan-Andromeda Archaeological Survey (PAndAS; McConnachie et al. 2009), have demonstrated that there is a significant amount of coherent substructure in the outer halo; these coherent streams indicate that M31's halo is currently being assembled by accretion of dwarf satellites. Ibata et al. (2014) present maps of the outer halo, demonstrating that there are a multitude of streams, plumes, and clouds of metal-poor stars, along with a

⋆Based on observations obtained with the Hobby–Eberly Telescope, which is a joint project of the University of Texas at Austin, the Pennsylvania State University, Stanford University, Ludwig-Maximilians-Universität München, and Georg-August-Universität Göttingen.

†E-mail: sakaricm@u.washington.edu
‡Present address: Department of Astronomy, University of Washington, Seattle, WA 98195-1580, USA.

§Vanier Canada Graduate Scholar.

significant metal-rich population that is mostly located in the Giant Stellar Stream (GSS) south of M31. As much as 42 per cent of the most metal-poor stars ([Fe/H] < -1.7) lie in coherent substructure – for metal-rich stars ([Fe/H] > -0.6) this percentage rises to 86 per cent. The rest of the outer halo stars are distributed in a 'smooth' component.

The presence of metal-rich and metal-poor coherent streams implies that M31 is currently accreting multiple dwarf satellites (see e.g. Johnston et al. 2008 for accretion simulations that lead to coherent streams). The locations and metallicities of the outer halo field stars can be used to infer the nature of these dwarf galaxies.

(i) The metal-rich GSS and the surrounding metal-rich features indicate that M31 has accreted at least one fairly massive [∼Large Magellanic Cloud (LMC) mass] galaxy (Ibata et al. 2001, 2007, 2014; Ferguson et al. 2002; Fardal et al. 2013). Star formation histories indicate that most of the metal-rich stars formed more than 5 Gyr ago, hinting that the progenitor may have been an early-type dwarf (Bernard et al. 2015).

(ii) Intermediate [Fe/H] stars are also found in coherent substructures, notably the SW cloud (Bate et al. 2014; Ibata et al. 2014), which has its own GCs (PA7, PA8, and PA14; Mackey et al. 2013, 2014) and possibly its own H I gas (Lewis et al. 2013). Estimates based on metallicity and total brightness suggest that the SW Cloud progenitor was also a fairly massive dwarf galaxy (with a mass comparable to the Fornax dwarf spheroidal; Bate et al. 2014).

(iii) The most metal-poor streams are gas-free (based on 21-cm observations; Lewis et al. 2013) and likely originated in lower mass dwarf spheroidal systems.

The outer halo GCs also suggest that M31 has had a fairly active accretion history. Of the ∼60 GCs discovered in PAndAS, many appear to lie along stellar streams. Mackey et al. (2010) demonstrated that the positions of these GCs are correlated with the positions of the streams, with a <1 per cent chance that these GCs are located along the streams by chance. PA7 and PA8 are kinematically associated with each other (Mackey et al. 2013) and with the SW Cloud itself (Bate et al. 2014; Mackey et al. 2014). Veljanoski et al. (2013, 2014) also show that many of the GCs which appear to lie along streams could be associated, based on their kinematics. Colucci, Bernstein & Cohen (2014) have also demonstrated that at least one outer halo GC (G002) has likely been accreted from a dwarf satellite.

Taken as a whole, the entire outer halo GC system is also different from the MW's GC population. For instance, Huxor et al. (2014) show that M31 has more luminous and faint GCs than the MW – they suggest that M31 could have acquired these extra GCs through accretion. Veljanoski et al. (2014) also demonstrate that the entire GC system has clear signs of rotation in both the GCs spatially associated with streams and those that are unassociated with streams. This rotation suggests either (1) that M31 experienced a merger with a galaxy large enough to bring in a substantial fraction of the outer halo GCs, or (2) that the parent dwarf galaxies were accreted from a preferred direction such that their angular momenta were correlated, as is presently seen for a separate plane of dwarf satellites (Ibata et al. 2013).

Ultimately, the observations of outer halo stars and GCs indicate that M31 has recently experienced a merger with at least one massive dwarf and multiple lower mass dwarfs. Detailed chemical abundances (from high-resolution spectroscopy) are an effective way to isolate and identify coeval groups, a process known as 'chemical tagging' (e.g. Freeman & Bland-Hawthorn 2002; Mitschang et al. 2014). With abundances of α, iron-peak, and neutron capture elements, metal-rich ([Fe/H] $\gtrsim -1.5$) stars and GCs from dwarf galaxies can be distinguished from those in massive galaxies (e.g. Venn et al. 2004; Tolstoy, Hill & Tosi 2009; Ting et al. 2012). Unlike GCs associated with the MW and its dwarf satellites, however, distant extragalactic targets must be observed through their IL. While metallicity and α-abundances can be determined from lower resolution IL spectra (e.g. Schiavon et al. 2002; Lee & Worthey 2005; Puzia, Kissler-Patig & Goudfrooij 2006; Puzia & Sharina 2008; Caldwell et al. 2011), the detailed chemical abundances necessary for chemical tagging analyses require high-resolution IL spectroscopy (see e.g. McWilliam & Bernstein 2008; Sakari et al. 2013). As in the MW (Cohen 2004; Sbordone et al. 2005; Sakari et al. 2011), if the M31 outer halo GCs originated in lower mass dwarf galaxies then they could have distinct abundance patterns from MW field stars, depending on metallicity.

High-resolution IL spectroscopy has been tested extensively on Galactic GCs (McWilliam & Bernstein 2008; Cameron 2009; Sakari et al. 2013, 2014), demonstrating that

(i) IL abundances trace the individual stellar abundances and represent cluster averages when abundances do not vary between stars;

(ii) abundance determinations from high-resolution IL spectroscopy are more precise than from lower resolution studies;

(iii) certain abundance ratios are very stable to uncertainties in the underlying stellar populations (e.g. interloping field stars, uncertainties in cluster age, microturbulence relations, etc.), such as [Ca/Fe];

(iv) partially resolved photometry down to the horizontal branch (HB) reduces systematic uncertainties by constraining [Fe/H] and HB morphology.

Thus, a high-resolution IL spectroscopic analysis of M31 GCs can provide precise and accurate abundances that will be suitable for chemical tagging. High-resolution IL spectroscopic techniques have been applied to nearby GCs in the Local Group (in M31, Colucci et al. 2009, 2014; the LMC, Colucci et al. 2011, 2012; and in dwarf galaxies, Colucci & Bernstein 2011) and in the large elliptical galaxy NGC 5128 (Colucci et al. 2013). At the distance of M31, the size and brightness of its GCs make them ideal targets for high-resolution IL spectroscopy.

This paper presents a high-resolution IL chemical tagging analysis of seven outer halo M31 GCs, five of which were first observed in PAndAS. This is the first chemical analysis for these five PAndAS clusters, at any resolution. Section 2 presents the data and the analysis methods, while Section 3 describes the process for generating synthetic stellar populations for each cluster. The IL abundances are given in Section 4, and the implications for the formation of M31's outer halo are then discussed in Section 5. Finally, the results are summarized in Section 6.

2 OBSERVATIONS AND ANALYSIS METHODS

2.1 Target selection

The primary goal of this high-resolution spectroscopic investigation of M31 GCs is to study the nature of the stars and clusters in M31's outer halo. The targets were therefore restricted to GCs with projected distances from the centre of M31 that are $R_{\rm proj} > 30$ kpc; priority was given to the GCs with the largest projected radii. Observational constraints required that the targets were sufficiently bright to observe in a reasonable amount of time and to avoid stochastic sampling issues – as a result, the target GCs are on the bright

Table 1. Properties of the target PAndAS clusters.

Cluster	RA (J2000)	Dec. (J2000)	$V_{\rm int}$	$R^{a}_{\rm proj}$ (kpc)	Photometric[b] [Fe/H]	Spatial association with stream?	References
H10	$00^{\rm h}35^{\rm m}59\overset{\rm s}{.}7$	$+35°41\$'\$03\overset{''}{.}6$	15.7	78.5	−1.84	N	1, 2
H23	$00^{\rm h}54^{\rm m}25\overset{\rm s}{.}0$	$+39°42\$'\$55\overset{''}{.}5$	16.8	37.1	−1.54	Stream D?	1, 2
PA06	$00^{\rm h}06^{\rm m}12\overset{\rm s}{.}0$	$+41°41\$'\$21\overset{''}{.}0$	16.5	93.7	MP	N	2, 3, 4
PA17	$00^{\rm h}26^{\rm m}52\overset{\rm s}{.}2$	$+38°44\$'\$58\overset{''}{.}1$	16.3	53.9	?[c]	N	2, 3
PA53	$01^{\rm h}17^{\rm m}58\overset{\rm s}{.}4$	$+39°14\$'\$53\overset{''}{.}2$	15.4	95.9	MP	N	2, 3, 4
PA54	$01^{\rm h}18^{\rm m}00\overset{\rm s}{.}1$	$+39°16\$'\$59\overset{''}{.}9$	15.9	95.8	MP	N	2, 3, 4
PA56	$01^{\rm h}23^{\rm m}03\overset{\rm s}{.}5$	$+41°55\$'\$11\overset{''}{.}0$	16.8	103.3	MP	N	2, 3, 4

References: 1 – Mackey et al. (2007); 2 – Veljanoski et al. (2014); 3 – Huxor et al. (2014); 4 – Mackey et al. (in preparation).

[a]Projected distances are from the centre of M31.

[b]Photometric metallicity estimates are used to constrain the parameters of the input isochrones; see Section 3. [Fe/H] estimates are based on Galactic GC fiducial fits. MP indicates a metal-poor cluster ([Fe/H] $\lesssim -1.5$); fiducial fits will be given in Mackey et al. (in preparation).

[c]PA17 does not have an *HST* CMD, and there is therefore no a priori information about its metallicity or HB morphology.

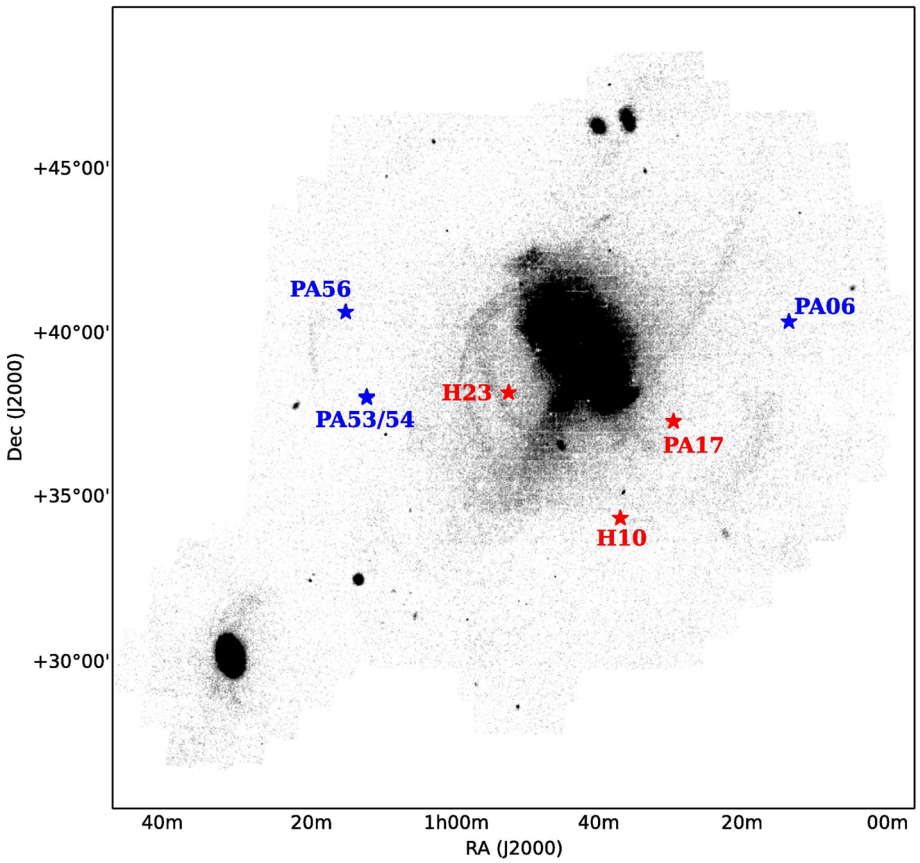

Figure 1. Locations of the target PAndAS clusters on a metal-poor density map of the full PAndAS footprint. The locations of stellar streams and satellite galaxies are obvious as dark regions. The red stars show the metal-rich ([Fe/H] $\gtrsim -1.5$; see Section 4) PAndAS clusters observed in this paper, while the blue stars show the metal-poor GCs. Note that PA53 and PA54 are very close together in projection and share a single point in the plot.

end of the M31 outer halo GC distribution (see Huxor et al. 2014). Seven outer halo GCs were targeted; their properties are summarized in Table 1. Two of these target clusters (H10 and H23) were discovered by Huxor et al. (2008); the other five were discovered in the PAndAS programme (Huxor et al. 2014). The locations of these GCs on a density map of metal-poor outer halo stars (from Irwin, private communication) are shown in Fig. 1. Note that none of the targets falls precisely on to any of the major stellar streams or overdensities in the outer halo. Nonetheless, PA56 sits on a faint north-western extension of the eastern cloud, and is likely associated with this feature (Mackey et al., in preparation). While H23 has been tentatively linked to Stream D based on its relative proximity in projection (Mackey et al. 2010), its radial velocity renders a genuine association unlikely (Veljanoski et al. 2014).

Table 2. PAndAS cluster observations.

Cluster	Observation dates	Exposure time (s)	S/N[a] (5500 Å)	S/N[a] (7000 Å)	$r_{\rm ILS}^{b}$ ($r_{\rm h}$)	$v_{\rm helio,\,obs}$ (km s^{-1})	$v_{\rm helio,\,lit}$ (km s^{-1})	$\sigma_{\rm obs}$ (km s^{-1})
H10	2011 Jan 2, 10, 11, 22, 23, 28, 30	19 180	82	140	2.3	-351.9 ± 1.5	-352 ± 9	6.6 ± 0.4
H23	2011 July 5, 7, 10, 11; Aug 2, 4; Sep 23	16 050	65	82	4.1	-373.3 ± 0.1	-377 ± 11	6.2 ± 0.4
PA06	2011 Sep 29; Oct 1, 2, 4, 6, 17, 18, 19, 21, 23	29 278	65	105	2.6	-341.4 ± 0.7	-327 ± 15	5.6 ± 0.4
PA17	2012 Jan 16, 18, 21	8100	41	50	2.6	-260.0 ± 1.0	-279 ± 15	6.1 ± 0.5
PA53	2011 Aug 1; Sep 20, 26	8100	115	148	2.7	-270.8 ± 0.9	-253 ± 10	12.0 ± 0.4
PA54	2011 Aug 25; Sep 24, 25, 27	10 800	82	130	2.2	-344.9 ± 0.8	-336 ± 8	7.5 ± 0.4
PA56	2011 Oct 7, 17, 18, 20, 21, 23, 24, 30; Nov 19; Dec 30 2012 Feb 10, 11	30 623	65	82	2.4	-241.4 ± 1.7	-239 ± 8	6.4 ± 0.4

References: literature radial velocities are from Veljanoski et al. (2014).
[a]S/N ratios are per resolution element, and assume that there are 2.7 pixels per resolution element for HRS.
[b]The coverage radii are based on the half-light radii in Tanvir et al. (2012) and Huxor et al. (2014) – all GCs are covered past their half-light radii.

Sakari et al. (2014) present detailed tests of systematic abundance errors that occur because of uncertainties in the underlying stellar populations. These tests include

(i) uncertainties in isochrone parameters such as age and [Fe/H];
(ii) properties of evolved HB and asymptotic giant branch (AGB) stars, particularly the HB morphology;
(iii) assumptions about the stellar populations [e.g. microturbulence relations, initial mass functions (IMFs), mass segregation];
(iv) unusual stars like interloping field stars, long period variables, etc.

These errors can be mitigated if GC properties are constrained with photometry or lower resolution analyses over a broader wavelength range. Observing priority was therefore given to those targets with partially resolved photometry. Six of the seven target GCs have *Hubble Space Telescope* (*HST*) photometry down to the HB (Mackey et al. 2007; Mackey et al., in preparation). This photometry is used to place constraints on the best-fitting isochrones (see Section 3).

2.2 Observations and data reduction

The targets were observed with the Hobby–Eberly Telescope (HET; Ramsey et al. 1998; Shetrone et al. 2007) at McDonald Observatory in Fort Davis, TX in 2011 and early 2012. The High Resolution Spectrograph (HRS; Tull 1998) was utilized with the 3-arcsec fibre and a slit width of 1 arcsec, yielding an instrumental spectral resolution of $R = 30\,000$. With the 600 g mm^{-1} cross-disperser set to a central wavelength of 6302.9 Å, wavelength coverages of ∼5320–6290 and ∼6360–7340 Å were achieved in the blue and the red, respectively. The 3-arcsec fibre provided coverage of the clusters past their half-light radii; the additional sky fibres (located 10 arcsec from the central object fibre) provided simultaneous observations for sky subtraction. Exposure times were calculated to obtain a total signal-to-noise ratio (S/N) = 80 (per resolution element), although not all targets received sufficient time to meet this goal. The details of the observations are shown in Table 2.

Data reduction was performed in the Image Reduction and Analysis Facility (IRAF) program.[1] As in Sakari et al. (2013), bias removal was not performed to avoid adding noise to the individual spectra, and variance weighting was used during aperture extraction to remove cosmic rays. Sky spectra (from the separate sky fibres) were replaced with continuum fits with the emission lines added back in [according to the sky line identifications from the Ultraviolet and Visual Echelle Spectrograph (UVES) quality control sky spectrum website; Hanuschik 2003][2] and were then subtracted from the object spectra. Telluric standards were also observed for removal of atmospheric absorption features.

In order to avoid removing broad, blended features, the target spectral orders were normalized with continuum fits to an extremely metal-poor star (CS 29502−092; see Sakari et al. 2013). Low-order polynomial fits were then necessary to fully normalize the target spectra. The individual observations were cross-correlated with a high resolution, high S/N Arcturus spectrum (from the Arcturus Atlas;[3] Hinkle et al. 2003) to determine radial velocities. Heliocentric velocities were determined for each individual observation; the final, averaged heliocentric velocities are shown in Table 2. The quoted errors represent the dispersion between observations.

The individual, rest-frame spectra were combined with average σ-clipping rejection routines to remove any remaining cosmic rays; each spectrum was weighted by flux during the combination. The combined spectra were once again cross-correlated with the Arcturus template spectrum to determine cluster dispersions (see Sakari et al. 2013 for a description of how this is done). These velocity dispersions are also shown in Table 2. Examples of the final, combined spectra are shown in Fig. 2.

2.3 Line list and EW measurements

For these chemical tagging analyses, spectral lines of Fe, Na, Mg, Ca, Ti, Ni, Ba, and Eu are utilized. Sakari et al. (2013, 2014) demonstrated that for Galactic GCs reliable Fe, Ca, Ti, Ni, and Ba abundances can be determined from equivalent widths (EWs), while Na, Mg, and Eu abundances can be determined with spectrum syntheses. Note that in this analysis the Ba lines are synthesized instead of using EWs, due to the lower S/N ratios of the target spectra.

[1] IRAF is distributed by the National Optical Astronomy Observatory, which is operated by the Association of Universities for Research in Astronomy, Inc., under cooperative agreement with the National Science Foundation.

[2] http://www.eso.org/observing/dfo/quality/UVES/pipeline/sky_spectrum.html
[3] ftp://ftp.noao.edu/catalogs/arcturusatlas/

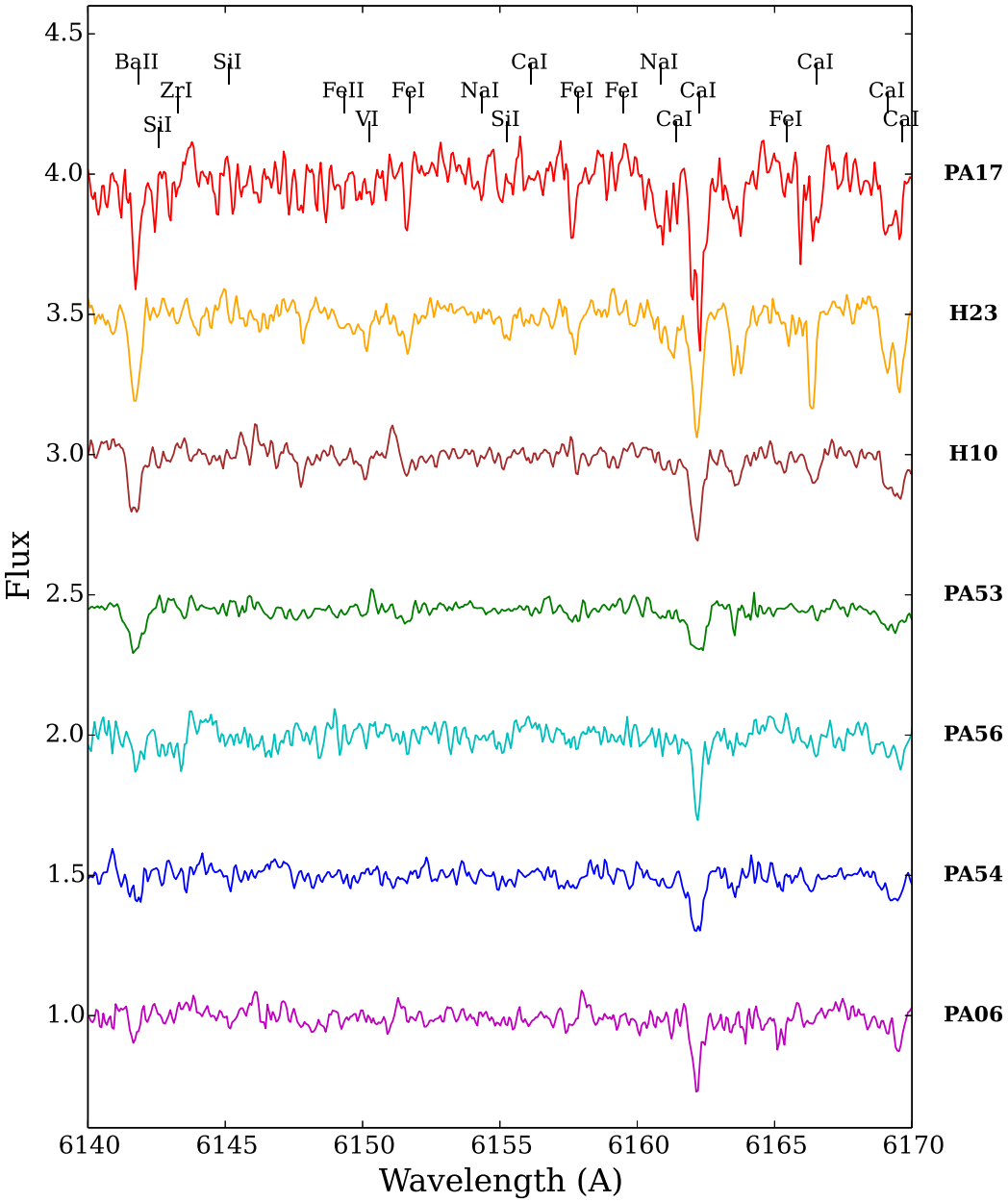

Figure 2. IL spectra of the PAndAS GCs, arranged by metallicity. Spectral lines used in typical RGB stellar analyses are identified.

EWs for Fe, Ca, Ti, and Ni lines were measured with the program DAOSPEC[4] (Stetson & Pancino 2008). Sakari et al. (2013) verified that DAOSPEC measurements of IL spectral lines compare well with measurements from other methods for GCs with a range of velocity dispersions. Given the low S/N of some of the PAndAS targets, many of the DAOSPEC EWs were verified or refined by hand. IL spectral lines have contributions from stars with a variety of line strengths – in particular, IL lines with EWs $\gtrsim$ 100 mÅ can have contributions from bright red giant stars with EWs $\sim$200 mÅ. These strong lines are difficult to model (see the discussions in Sakari et al. 2013 and McWilliam et al. 1995) and are typically removed from individual stellar analyses. For this reason, as a conservative estimate, all lines stronger than $\sim$110 mÅ were removed from this analysis unless absolutely necessary.

Table 3 shows the spectral lines that were used to derive abundances in the analysis, their atomic data, and the measured IL EWs for each cluster. The line list is based on the standard IL lines lists of McWilliam & Bernstein (2008) and Colucci et al. (2009), with supplements from the red giant branch (RGB) stellar line lists of Sakari et al. (2011) and Venn et al. (2012). Lines that were measured with spectrum syntheses are indicated. The full line lists to synthesize all lines in a 10 Å window (for spectrum syntheses) are the ones used in Sakari et al. (2013): they consist of the EW line list, with supplements from the Vienna Atomic Line Database[5] (VALD;

[4] DAOSPEC has been written by P. B. Stetson for the Dominion Astrophysical Observatory of the Herzberg Institute of Astrophysics, National Research Council, Canada.

[5] http://www.astro.uu.se/~vald/php/vald.php

Table 3. The line list.[a]

λ (Å)	Element	E.P. (eV)	log gf	Equivalent width (mÅ)						
				H10	H23	PA06	PA17	PA53	PA54	PA56
5324.191	Fe I	3.21	−0.103	–	–	80.0	–	83.1	79.4	80.0
5339.937	Fe I	3.27	−0.720	81.0	–	–	–	–	–	54.8
5367.476	Fe I	4.42	0.443	77.9	93.9	46.0	–	68.0	50.0	53.2
5369.974	Fe I	4.37	0.536	–	–	50.0	–	–	–	59.4
5371.501	Fe I	0.96	−1.644	–	–	126.0	–	–	–	–

Notes. Equivalent widths were measured in DAOSPEC; all strong lines were checked and refined in *splot*. IL lines stronger than 110 mÅ were not included in the analysis.
[a]This table is published in its entirety in the electronic edition of the journal. A portion is shown here for guidance regarding its form and content.

Kupka et al. 2000), the Kurucz data base,[6] and the National Institute of Standards and Technology (NIST)[7] data base. Molecular features from the Kurucz data base were included when indicated in the Arcturus Atlas (for CH, CN, and MgH). Isotopic and hyperfine structure (HFS) components for the Ba II lines are from McWilliam (1998) while the Eu II components are from Lawler, Bonvallet & Sneden (2001a) and Lawler et al. (2001b). The HFS components are included in the syntheses; while they do not significantly affect the strengths of the lines, they can affect the line profiles.

2.4 Solar abundances

Sakari et al. (2013, 2014) presented measurements of the solar spectrum from the Kurucz (2005) solar flux atlas.[8] The [Fe/H] and [X/Fe] ratios in this paper were calculated *line by line* using the solar abundances derived from those EWs and spectrum syntheses. When the solar lines were stronger than 150 mÅ, Asplund et al. (2009) solar abundances were adopted for those lines.

3 UNDERLYING STELLAR POPULATIONS

The first step in an IL analysis is to determine the atmospheric parameters of the stars in the underlying populations. The central regions of the PAndAS GCs cannot be resolved with *HST*, and high-quality colour-magnitude diagrams (CMDs) cannot be obtained for the regions included in the IL spectra – isochrones must therefore be used to model the stellar populations. Synthetic populations are generated with the BaSTI isochrones (Pietrinferni et al. 2004; Cordier et al. 2007) with extended AGBs and mass-loss parameters of $\eta = 0.2$, assuming a Kroupa (2002) IMF and the total cluster magnitudes from Huxor et al. (2014). The BaSTI isochrones are utilized because they extend all the way through the AGB phase – Sakari et al. (2014) show that differences between isochrone sets are insignificant for the abundances derived in this paper. The synthetic Hertzsprung–Russell Diagram (HRD) populations are binned into boxes, each with 3.5 per cent of the total flux. The boxes are then assigned corresponding Kurucz model atmospheres[9] (Castelli & Kurucz 2004), where the grid values are interpolated to a specific box's $T_{\rm eff}$ and $\log g$. When the [Ca/Fe] ratio is supersolar, α-enhanced model atmospheres are used. Microturbulent velocities are determined via an empirical relation between ξ (in km s^{-1}) and $\log g$ that fits the Sun and Arcturus (see McWilliam & Bernstein 2008).

The abundances of the Fe I lines (from the EWs in Table 3) are used to constrain the best-fitting isochrone's single age and metallicity. As in McWilliam & Bernstein (2008) and Colucci et al. (2009, 2011, 2013), the adopted isochrone is the one that leads to the flattest trends in Fe I abundance with wavelength, reduced EW (REW),[10] and excitation potential (EP); these criteria are adopted from analyses of individual stars (see McWilliam & Bernstein 2008).

3.1 Clusters with *HST* photometry

The stars in the outer regions of six of the targets clusters have been resolved with *HST*, enabling constraints to be placed on the GC [Fe/H] and HB morphology.[11] This photometry is not used to identify the isochrone that best fits the resolved CMD, but is only used to constrain the possible isochrones and HB morphology. These constraints help to drastically reduce the systematic errors in the IL abundances (see Sakari et al. 2014). For the blue HB clusters (PA06, PA53, PA54, and PA56; see Fig. 3), synthetic BaSTI HBs[12] are used instead of the default HBs. Sakari et al. (2014) show that as long as the HBs are modelled approximately correctly the integrated abundances will not be systematically affected.

The parameters of the spectroscopically determined isochrones are listed in Table 4 and the isochrones themselves are shown on top of the observed CMDs in Fig. 3 (for the six clusters with *HST* photometry). Again, *these isochrones were not derived based on fits to the observed CMDs*, but were determined by minimizing trends in the Fe I line abundances. The fact that the isochrones agree well with the CMDs confirms the validity of these high-resolution IL techniques.

The slopes of the trends in Fe I abundances are given in Table 5. Again, solutions were selected by simultaneously minimizing trends in Fe I abundance with wavelength, REW, and EP. All REW and EP trends for the PAndAS clusters are flat within their 1σ errors. The line-to-line dispersion can still be quite large, which leads to some uncertainty in isochrone age (∼5 Gyr), though this has a minimal effect on the integrated abundances (Sakari et al. 2014). Also note that the BaSTI isochrones have large spacings in metallicity (∼0.2–0.3 dex, depending on [Fe/H]), preventing exact metallicities from

[6] http://kurucz.harvard.edu/linelists.html
[7] http://www.nist.gov/index.html
[8] http://kurucz.harvard.edu/sun.html
[9] http://kurucz.harvard.edu/grids.html

[10] REW = EW/λ.
[11] Rough constraints can also be placed on cluster age, specifically whether the cluster is older than ∼4 Gyr; additionally, the presence of RR Lyrae stars would constrain the age to >10 Gyr.
[12] http://basti.oa-teramo.inaf.it/BASTI/WEB_TOOLS/HB_SYNT/index.html

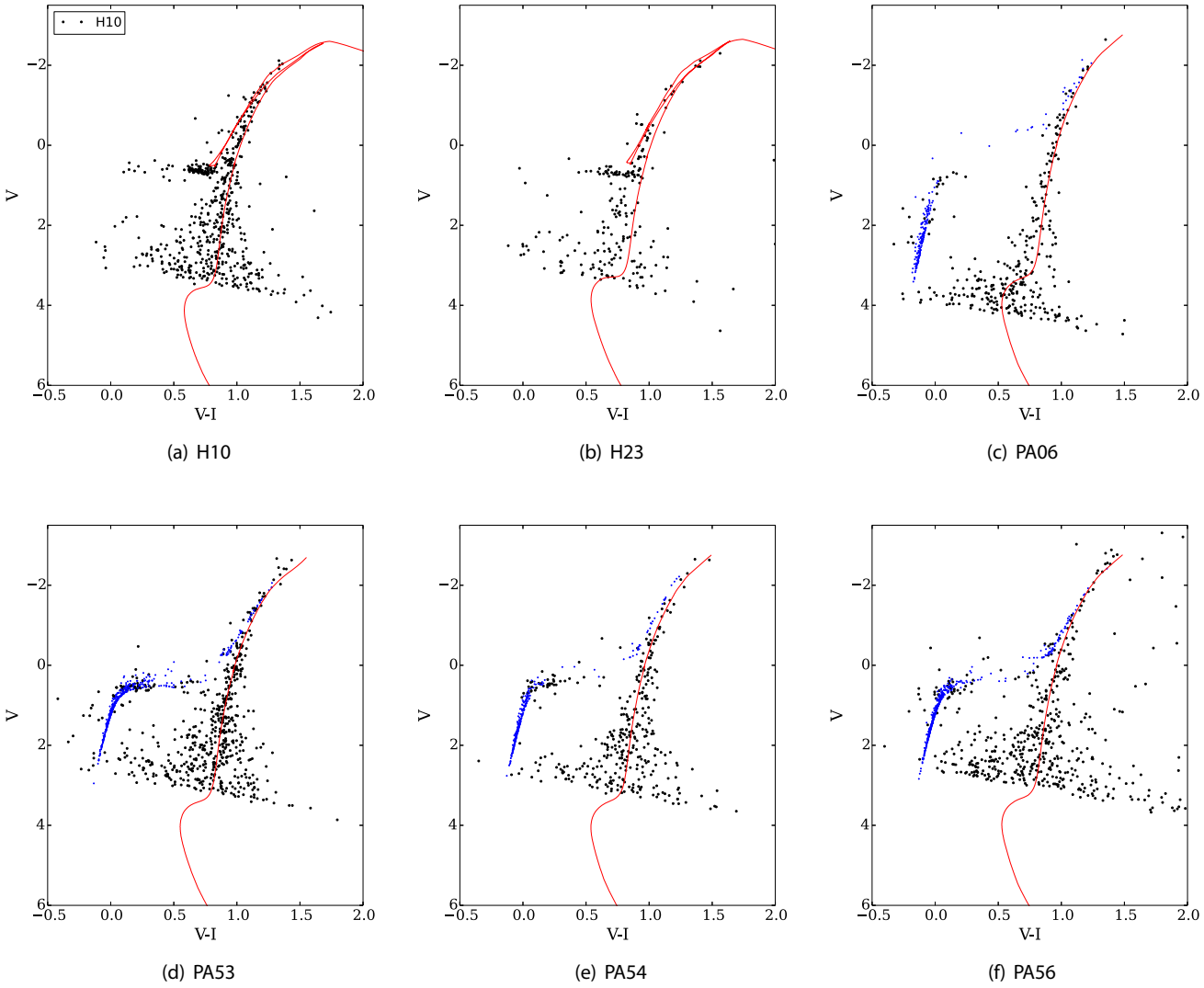

Figure 3. *HST* CMDs of the six partially resolved PAndAS GCs. The spectroscopically determined best-fitting isochrones are shown (in red) on the CMDs to illustrate how the synthetic HRDs are populated. For the blue HB clusters PA06, PA53, PA54, and PA56, synthetic HBs (shown in blue) were used instead of the default HBs.

Table 4. Parameters of the 'best-fitting' HRDs and synthetic and observed integrated colours.

	Isochrone [Fe/H]	Age (Gyr)	Synthetic $(V-I)_0$	Observed[a] $(V-I)_0$	$\Delta(V-I)_0$
H10	−1.31	12	0.94	0.95	−0.01
H23	−1.31	9	0.98	1.01	−0.03
PA06	−1.84	12	0.91	0.87	+0.04
PA17[b]	−1.01	12	1.05	1.14	−0.09
PA53	−1.62	12	0.89	0.85	+0.04
PA54	−1.84	13	0.89	0.84	+0.05
PA56	−1.62	12	0.88	0.89	−0.01

[a]Uncertainties in the observed colours from Huxor et al. (2014) are likely to be ∼0.05 dex.
[b]PA17 does not yet have a high-quality *HST* CMD; therefore, there are few a priori constraints on the underlying stellar population.

Table 5. Trends in Fe I abundance for the PAndAS clusters.

Cluster	Wavelength slope (10^{-5} dex Å^{-1})	REW slope (dex)	EP slope (dex eV^{-1})
H10	2.7 ± 4.0	−0.030 ± 0.097	−0.011 ± 0.019
H23	−1.5 ± 2.9	−0.016 ± 0.067	−0.0020 ± 0.015
PA06	−1.8 ± 2.3	−0.0057 ± 0.058	0.0041 ± 0.011
PA17[a]	3.3 ± 7.5	0.035 ± 0.19	0.015 ± 0.029
PA53	3.7 ± 5.7	0.019 ± 0.18	0.019 ± 0.025
PA54	9.3 ± 3.7	−0.00018 ± 0.099	−0.020 ± 0.020
PA56	6.8 ± 5.6	0.033 ± 0.13	0.0081 ± 0.026

[a]PA17 does not yet have a high-quality *HST* CMD; therefore, there are few a priori constraints on the underlying stellar population.

being adopted for the isochrones. Comparisons with the integrated colours are shown in Table 4. The differences for the six partially resolved GCs are all $\lesssim$0.05 mag (which is the approximate uncertainty in the observed colours from Huxor et al. 2014); this indicates that the populations are at least reasonably well modelled. H10 and H23's slightly redder synthetic colours may be due to the fact that the default HBs are slightly too red (see Figs 3a and b), while the inconsistencies in the other GCs might be due to incorrect ages or slight discrepancies in the RGBs, HBs, or AGBs.

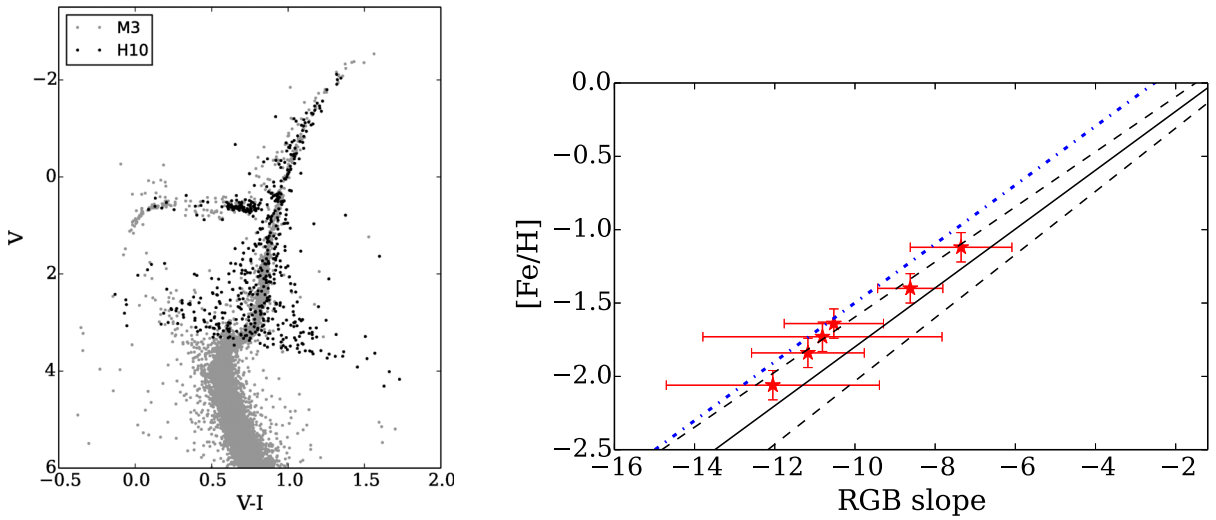

Figure 4. Left: the H10 *HST* CMD, plotted on M3's *V*, *I* CMD from the ACS Globular Cluster Survey (Sarajedini et al. 2007; Anderson et al. 2008). The distance modulus and reddening have been adjusted to match the HBs of the two clusters. The slopes of the GCs agree well, supporting the higher spectroscopic metallicity from this study. Right: RGB slopes (determined from the *HST* photometry) versus spectroscopic metallicity. The solid line shows the calibration with Galactic GCs (presented in Appendix A), while the red stars show the slopes of the PAndAS clusters. The RGB slopes predict metallicities that agree well with the integrated [Fe/H] values. The blue dot–dashed line shows the offset that would occur at a fixed [Fe/H] if clusters have $[\alpha/\mathrm{Fe}] = 0$ (see Appendix A).

3.2 PA17: the cluster without *HST* photometry

Since PA17 does not yet have a high-quality *HST* CMD there is little a priori information available to constrain its age, [Fe/H], or HB morphology. As a result the isochrone default HBs were used. The flattest slopes occur for a relatively metal-rich isochrone, with [Fe/H] ~ -1, and an age of 12 Gyr. Given PA17's [Fe/H] and red integrated colour ($(V-I)_0 = 1.14$, which is redder than H10 and H23; Huxor et al. 2014), the default BaSTI HB (which is red) is likely to be sufficient, and there abundance offsets as a result of the uncertain HB morphology should be negligible. With the default HBs, the Fe I abundances imply a best-fitting age and [Fe/H] of 12 Gyr and -1.01, respectively, for PA17.

3.3 Comparisons with literature values

H10's isochrone age and integrated [Fe/H] agree well with the high-resolution IL values from Colucci et al. (2014), which are determined from spectra with a slightly different wavelength range. However, the metallicities and ages for H10 and H23 from this work do not agree with the previous photometric results from Mackey et al. (2007). From analyses of partially resolved CMDs of the upper RGBs, Mackey et al. (2007) find [Fe/H] values for H10 and H23 that are lower than the integrated [Fe I/H] ratios presented here. The fiducial fits in Mackey et al. are performed with an optimization routine that finds the best combination of Galactic GC fiducial (at a given [Fe/H]), distance modulus, and reddening that fit the observed RGB. This should provide a good estimate of cluster [Fe/H], since the slope of the RGB is primarily sensitive to metallicity (e.g. Sarajedini 1994), though this [Fe/H] is dependent on the adopted distance modulus and reddening. For instance, Mackey et al. (2007) find that H10's RGB falls between the fiducials of M92 ([Fe/H] $= -2.14$) and NGC 6752 ([Fe/H] $= -1.54$), implying that H10 likely has a metallicity of [Fe/H] ≈ -1.84. However, Fig. 4(left) demonstrates that H10's RGB slope can be well represented by M3's RGB, indicating a higher metallicity of [Fe/H] ≈ -1.5 (which agrees with the spectroscopic values from this work).

A similar technique can be applied to all the PAndAS GCs. An empirical calibration between Galactic GC RGB slope (in the *F606W* and *F814W HST* filters) is provided in Appendix A. The RGB slopes and metallicities of the PAndAS GCs are shown in Fig. 4(right) on top of this empirical Galactic GC relation. The cluster HBs were first aligned with 47 Tuc and/or M3 to fix the distance modulus and reddening. The approximate $(V-I)_0$ colours at two fixed absolute magnitudes ($M_V = 0$ and $M_V = -2$) were then determined, and RGB slopes were calculated. The approximate uncertainties in RGB slope are estimated from the uncertainties in RGB colour and distance modulus – note that PA56 has a large uncertainty because its paucity of bright HB stars makes its distance modulus more uncertain. The quoted errors in [Fe/H] are 0.1 dex, to reflect possible systematic errors (Sakari et al. 2014). The PAndAS GCs agree with the Galactic GC relation within the 1σ errors; however, all the PAndAS GCs have slightly steeper slopes than their Galactic counterparts, hinting that the clusters may be α-deficient compared to the calibrating MW GCs (see the discussion in Appendix A). Regardless, this general agreement shows that the spectroscopic metallicities derived in this paper are consistent with the observed CMDs.

4 ABUNDANCES

Abundances were determined with ILABUNDS (first introduced in McWilliam & Bernstein 2008), an IL modification of the 1997 version of the local thermodynamical equilibrium (LTE) line analysis code MOOG (Sneden 1973). The final IL abundances[13] for all elements are shown in Table 6. Random errors for EW-based abundances are calculated as in Shetrone et al. (2003) and Sakari et al. (2011), where the largest of three errors was adopted: the line-to-line scatter for that element, the error due to EW uncertainties, or

[13] The standard notation is used, i.e.

$$[\mathrm{X/H}] = \log\epsilon(\mathrm{X}) - \log\epsilon(\mathrm{X})_\odot = \left(12 + \log\frac{N_\mathrm{X}}{N_\mathrm{H}}\right) - \left(12 + \log\frac{N_\mathrm{X}}{N_\mathrm{H}}\right)_\odot,$$

where N_X is the column density of any element X.

Table 6. Integrated abundances of the PAndAS clusters, with random errors and the number of lines for each element.

	PA17	H23	H10	PA53	PA56	PA54	PA06
[Fe I/H]	−0.93 ± 0.03	−1.12 ± 0.02	−1.36 ± 0.02	−1.64 ± 0.03	−1.73 ± 0.03	−1.84 ± 0.02	−2.06 ± 0.02
N	31	65	45	29	40	32	30
[Fe II/H]	−0.96 ± 0.15	−1.21 ± 0.08	−1.30 ± 0.04	−1.68 ± 0.10	−1.71 ± 0.10	−1.75 ± 0.08	−2.09 ± 0.10
N	4	5	5	1	1	2	1
[Na I/Fe I]	0.60 ± 0.15	−0.01 ± 0.23	0.35 ± 0.25	0.41 ± 0.30	0.43 ± 0.20	0.78 ± 0.30	0.71 ± 0.25
N	2	2	1	1	2	2	2
[Mg I/Fe I]	0.80 ± 0.15	0.30 ± 0.20	0.43 ± 0.15	0.20 ± 0.20	0.54 ± 0.15	0.32 ± 0.18	0.14 ± 0.20
N	1	2	2	1	2	2	1
[Ca I/Fe I]	0.04 ± 0.07	0.41 ± 0.04	0.25 ± 0.04	0.19 ± 0.03	0.24 ± 0.05	0.28 ± 0.04	0.46 ± 0.07
N	4	6	10	10	8	9	9
[Ti I/Fe I]	0.0 ± 0.10	0.56 ± 0.05	0.39 ± 0.10	0.16 ± 0.10	0.23 ± 0.10	–	–
N	1	3	1	1	1	0	0
[Ti II/Fe II]	0.17 ± 0.10	0.39 ± 0.10	0.40 ± 0.03	0.17 ± 0.06	–	0.49 ± 0.10	0.31 ± 0.10
N	1	1	2	2	0	1	2
[Ni I/Fe I]	−0.08 ± 0.09	−0.07 ± 0.04	0.01 ± 0.04	−0.11 ± 0.18	−0.10 ± 0.16	−0.05 ± 0.06	−0.02 ± 0.06
N	3	5	7	2	2	3	2
[Ba II/Fe II]	0.21 ± 0.25	−0.03 ± 0.11	−0.05 ± 0.11	0.03 ± 0.22	−0.39 ± 0.15	−0.10 ± 0.20	−0.17 ± 0.20
N	2	2	2	2	1	1	1
[Eu II/Fe II]	0.36 ± 0.35	0.53 ± 0.25	0.75 ± 0.20	0.68 ± 0.25	0.96 ± 0.15	<0.50	<1.04
N	1	1	1	1	1	1	1

Notes. [Fe/H] and [X/Fe] ratios are calculated differently, *line by line*, relative to the solar abundances for that line (see Sakari et al. 2013, 2014 for the EWs used to derive the solar abundances).

the iron line-to-line scatter. The largest of these three uncertainties is adopted as the final *random* abundance error for that element. Random errors for abundances derived via spectrum syntheses are calculated based on uncertainties in continuum placement *and* line profile fitting (see Sakari et al. 2013).

Systematic errors are adopted from Sakari et al. (2014), based on GC [Fe/H] and HB morphology. The optimal abundance ratios for chemical tagging are those which

(i) are least sensitive to uncertainties in the underlying stellar populations;
(ii) are most distinct between massive and dwarf galaxies.

Sakari et al. determined that the most stable and useful abundance ratios were [Ca I/Fe I], [Ni I/Fe I], and [Ba II/Eu II]. The first two [X/Fe] ratios are typically stable (within ∼0.1 dex) to most systematic uncertainties in the underlying populations. Though individually [Ba II/Fe II] and [Eu II/Fe II] are highly sensitive to the underlying stellar populations, the Ba II and Eu II offsets are often similar, and the [Ba/Eu] ratio is much more stable to population uncertainties (in a partially resolved system the uncertainties can still be as high as ∼0.1 dex). These ratios are also useful for comparisons with dwarf galaxy stars. The [Ca/Fe] ratio can serve as an [α/Fe] indicator, since metal-rich dwarf galaxy stars have lower [Ca/Fe] at a given [Fe/H] (see e.g. Tolstoy et al. 2009). The [Ni/Fe] ratio has been observed to be low in metal-rich field stars and clusters associated with the Sagittarius (Sgr) dwarf spheroidal (Cohen 2004; Sbordone et al. 2005, 2007) and anomalous MW field stars that are suspected to have been accreted from dwarf galaxies (Nissen & Schuster 2010). Finally, the [Ba/Eu] ratio is observed to be high in dwarf galaxy stars (see e.g. Tolstoy et al. 2009). Other suitable, high precision ratios include [Eu/Ca] and [Mg/Ca]. Although the other element ratios ([Na I/Fe I], [Mg I/Fe I], [Ti I/Fe I], and [Ti II/Fe II]) are less stable to uncertainties in the underlying populations, their agreement (or disagreement) with other abundance ratios may prove useful.

Table 7 presents estimates of the maximum systematic errors in the integrated abundances of the PAndAS clusters. All errors estimates are based on the tables presented in Sakari et al. (2014), with the exception of Na and Mg, which were calculated in the same way. The errors are selected from Sakari et al. (2014) to match the metallicity and HB morphology of the cluster, as well as the analysis technique. The GCs H10, H23, PA06, PA53, PA54, and PA56 are partially resolved, which reduces the systematic errors considerably. At [Fe/H] ∼ −1.4, H10 is closest in [Fe/H] to M3, M13, and NGC 7006; its systematic uncertainties are therefore averages from the three clusters (though note that since all H10's HB stars are red, the hot star uncertainties are not included). H23 has a metallicity in between 47 Tuc and M3/M13/NGC 7006, and its quoted uncertainties are therefore an average of the 47 Tuc values and the mean M3/M13/NGC 7006 values. PA53, PA54, and PA56 are similar in [Fe/H] and HB morphology to M3, M13, and NGC 7006, and their averaged abundance offsets are therefore utilized. M15's systematic uncertainties are adopted for PA06. For PA17, the unresolved cluster, the systematic uncertainties of 47 Tuc were adopted (since PA17's [Fe/H] ∼ −0.9 is closest to 47 Tuc's [Fe/H] ∼ −0.8; see Sakari et al. 2013), assuming that the cluster is modelled with isochrones and that there are no constraints on the underlying population.

In the following subsections, each element type is discussed separately. The [Fe/H] and [X/Fe] ratios of the PAndAS GCs are plotted along with field stars in the MW and its dwarf satellites. There are no *detailed* abundances for M31 field stars, though there are medium-resolution α-abundances for four outer halo M31 stars (Vargas et al. 2014); however, M31 field star abundance patterns are likely similar to the MW, especially for metal-poor stars. The PAndAS clusters are also compared to integrated and averaged abundances from GCs in the MW, the inner halo of M31, and MW satellite galaxies.

4.1 Iron

The [Fe/H] abundances were determined with EWs, as described in Section 2.3. Because (1) there are fewer Fe II lines and (2) Fe II is more susceptible to systematic effects (Sakari et al. 2013), [Fe I/H] is adopted as the representative [Fe/H], despite potential non-LTE

Table 7. Systematic error estimates.

	|Δ[Fe/H]|					|Δ[X/Fe]|						|Δ[X/Y]|		
	Fe I	Fe II	Na I	Mg I	Ca I	Ti I	Ti II	Ni I	Ba II	Eu II	[Mg/Ca]	[Na/Mg]	[Ba/Eu]	[Eu/Ca]
PA17	0.19	0.21	0.21	0.27	0.13	0.16	0.17	0.07	0.23	0.13	0.16	0.15	0.13	0.11
H23	0.13	0.19	0.13	0.14	0.08	0.12	0.10	0.07	0.18	0.10	0.08	0.11	0.09	0.09
H10	0.09	0.15	0.11	0.07	0.05	0.08	0.08	0.07	0.09	0.08	0.04	0.10	0.07	0.10
PA53, PA54, PA56	0.11	0.16	0.13	0.08	0.05	0.08	0.11	0.08	0.10	0.09	0.05	0.11	0.11	0.10
PA06	0.20	0.13	0.10	0.08	0.07	0.11	0.09	0.07	0.16	0.10	0.07	0.10	0.12	0.12

Notes. Total errors are conservatively estimated by adding the individual errors from Sakari et al. (2014) in quadrature, based on the appropriate [Fe/H] and HB morphology.

(NLTE) effects. Note that for all clusters Fe I and Fe II are in reasonably good agreement. Three clusters, H10, H23, and PA17, are more metal rich than [Fe/H] $= -1.5$, while the other four are metal poor. The most metal-poor clusters all have fewer detectable lines ($\sim$30 Fe I lines and 1–2 Fe II lines) than the more metal-rich GCs, leading to larger random errors in [Fe/H].

Most GC systems in dwarf galaxies tend to be metal poor, with more massive dwarf galaxies possessing more metal-rich GCs (e.g. Peng et al. 2006). The comparatively high metallicities of H10, H23, and PA17 therefore suggest that they formed in a galaxy more massive than the Fornax (For) dwarf spheroidal. It is clear from Tables 1 and 6 that the metal-rich PAndAS GCs have smaller projected distances from the centre of M31 than the more metal-poor GCs. Based on a low-resolution survey of inner halo, bulge, and disc M31 GCs, Caldwell et al. (2011) found evidence for an abundance gradient in the inner regions of M31 – this gradient seems to flatten to [Fe/H] ~ -1.8 at distances $\gtrsim$2 kpc. H23 and PA17 are therefore more metal rich than expected given their large distance from the centre of M31; however, metal-rich field stars have been identified in streams in M31's outer halo (Ibata et al. 2014).

4.2 α-elements

The α-elements (Mg, Ca, and Ti) form primarily through captures of ^{4}He nuclei during hydrostatic burning in massive stars, while Fe forms both during core-collapse supernovae of massive stars and during the detonation of white dwarfs whose progenitors were lower mass stars. Comparisons between the abundances of α-elements and Fe versus [Fe/H] provide an indication of how the chemical contributions from different types of stars have changed in a specific environment. Because the trends in [α/Fe] with [Fe/H] differ between massive and dwarf galaxies, the abundance ratios can be used to link stars and/or GCs to their birth environments.

4.2.1 Magnesium

Magnesium abundances for the PAndAS GCs are presented in Table 6. For most clusters [Mg/Fe] is determined from the 5528 and 5711 Å lines – however, PA17's [Mg/Fe] is only determined from the 5711 Å line because its 5528 Å line is too strong; similarly, the 5711 Å line is too weak in the most metal-poor cluster, PA06, and in the GC with the highest velocity dispersion, PA53. Comparisons with MW, M31, and dwarf galaxy field stars and clusters are shown in Fig. 5. Field stars in the most massive, nearby, well-studied dwarfs that host GCs are also shown, including the LMC and the Sgr and Fornax dwarf spheroidals; lower mass galaxies such as Sculptor and Carina are not included since they do not have GCs. The average and/or integrated abundances of MW, M31, LMC, Sgr, and Fornax GCs are shown separately from the field stars. The unusual MW GCs Palomar 1 (Pal 1; Sakari et al. 2011) and Ruprecht 106 (Rup 106; Villanova et al. 2013) and the M31 GC G002 (Colucci et al. 2014) are given different symbols, since their chemical abundances indicate that they may have originated in dwarf galaxies (though their host galaxies have not yet been identified).

Note that star-to-star Mg variations have been observed in massive, metal-poor, Galactic GCs ([Fe/H] $\lesssim -1.2$; Carretta et al. 2009a); in those clusters, Mg variations can be as large as 0.5–1 dex (e.g. Sneden et al. 1997, 2004; Cohen & Melendez 2005). The most metal-poor PAndAS GC, PA06, has a low [Mg/Fe] ratio for its metallicity, similar to M15 (see Sakari et al. 2013); this suggests that strong star-to-star Mg variations may exist in PA06. The integrated [Mg/Fe] ratios in the other metal-poor GCs roughly agree with the Galactic GCs. The integrated Mg abundances of the Colucci et al. (2014) M31 GCs are systematically lower than the PAndAS GCs at the metal-poor end – however, this may be due to the masses of the observed clusters. Many of the Colucci et al. targets have larger velocity dispersions and higher total luminosities, indicating that they are more massive than these PAndAS GCs. If this is the case, the GCs in the Colucci et al. sample may harbour stronger Mg variations (e.g. Carretta et al. 2009a). Colucci et al. (2014) *do* find a correlation between integrated [Mg/Fe] and total M_V for the metal-poor GCs, such that the more massive GCs have lower integrated [Mg/Fe] – all five of the most metal-poor ([Fe/H] < -1.2) PAndAS GCs are consistent with the Colucci et al. relation for all GCs.

Because of their high metallicities the two most metal-rich PAndAS GCs, H23 and PA17, are not likely to host significant star-to-star variations in Mg, though they may host multiple populations (see Section 4.3.2). The [Mg/Fe] ratios of H10 and H23 agree with Galactic field stars. Note that H10's [Mg/Fe] is higher than the value presented by Colucci et al. (2014), which was derived from slightly different lines; considering random and systematic uncertainties, however, the two are consistent. PA17 has a [Mg/Fe] ratio of 0.8 dex, which is higher than most of the field stars and all of the GCs. The syntheses of PA17's 5711 Å line are shown in Fig. 6 – this line has a similar strength in all three exposures, suggesting that the line strength is not due to an improperly removed cosmic ray. Note that there are no other Mg I features in the observed spectrum (other than the strong 5528 Å line) to verify this high abundance. With its high [Mg/Fe], PA17 falls at the upper end of the Galactic and LMC field stars. This high [Mg/Fe] ratio suggests a greater contribution from massive star ejecta, either from a top-heavy IMF or from inhomogeneous mixing and stochastic sampling of supernova ejecta. Alternatively, high Mg could indicate contributions from a

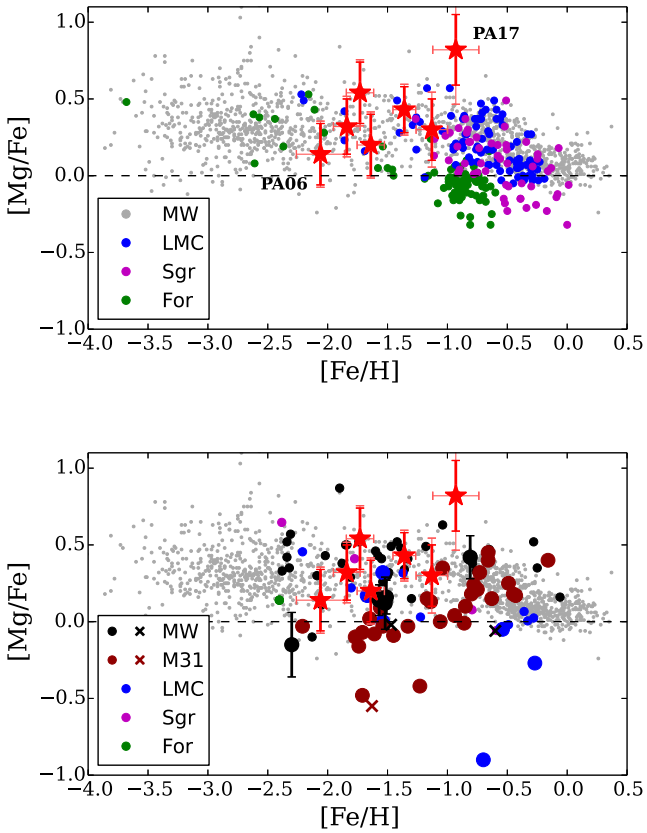

Figure 5. Top: comparisons of PAndAS clusters (red stars) to MW field stars (grey; from the sources in Venn et al. 2004, with supplements from Reddy, Lambert & Prieto 2006) and dwarf galaxy field stars. LMC stars are shown in blue (Pompéia et al. 2008), Sgr in magenta (Monaco et al. 2007; Sbordone et al. 2007; Carretta et al. 2010; Chou et al. 2010; McWilliam, Wallerstein & Mottini 2013), and Fornax (For) in green (Shetrone et al. 2003; Letarte et al. 2010; Tafelmeyer et al. 2010). The error bars show the random errors. The dashed horizontal line shows the solar value. Random errors are shown as thick error bars, while systematic and random errors (added in quadrature) are shown with the thinner error bars. Bottom: comparisons of PAndAS clusters (red stars) to MW field stars (grey), MW clusters (black circles), other M31 clusters (maroon), and dwarf galaxy GCs. IL abundances are shown as larger symbols, while averaged GC abundances from individual stars are shown as smaller symbols. IL abundances of MW clusters are from Sakari et al. (2014), while cluster averages are from Pritzl, Venn & Irwin (2005). The M31 cluster IL abundances are from Colucci et al. (2009, 2014). LMC clusters are in blue; IL abundances are from Colucci et al. (2012), while the individual stellar abundances are from Johnson, Ivans & Stetson (2006) and Mucciarelli et al. (2008). Average abundances of Sgr clusters are from Cohen (2004), Sbordone et al. (2005), and Mottini, Wallerstein & McWilliam (2008). Averages of the individual stars in Fornax clusters are in green, and are from Letarte et al. (2006). The unusual MW clusters Pal 1 and Rup 106 (from Sakari et al. 2011 and Villanova et al. 2013) and the M31 GC G002 (from Colucci et al. 2014) are shown with crosses – these GCs may have been accreted from dwarf galaxies, though they have no obvious host galaxies.

rapidly rotating massive star that went supernova (e.g. Takahashi, Umeda & Yoshida 2014).

4.2.2 *Calcium and titanium*

Calcium and titanium mainly form explosively in core-collapse supernovae and generally behave like the other α-elements, though both elements also form in Type Ia supernovae (Nomoto, Thielemann & Yokoi 1984; Maeda et al. 2010). The integrated [Ca I/Fe I] abundances are determined based on EWs of $\lesssim$10 spectral lines. All Ca I line EWs were verified by hand, and any uncertain lines were removed from the analysis. Spectrum syntheses were also performed on several Ca I lines to verify the EW-based abundances. The Ti abundances are based on fewer lines (1–3), but both [Ti I/Fe I] and [Ti II/Fe II] generally agree with [Ca/Fe]. Sakari et al. (2014) determined that the [Ti/Fe] ratios are more sensitive to systematic uncertainties in the underlying stellar populations; thus, only [Ca/Fe] is compared with other targets.

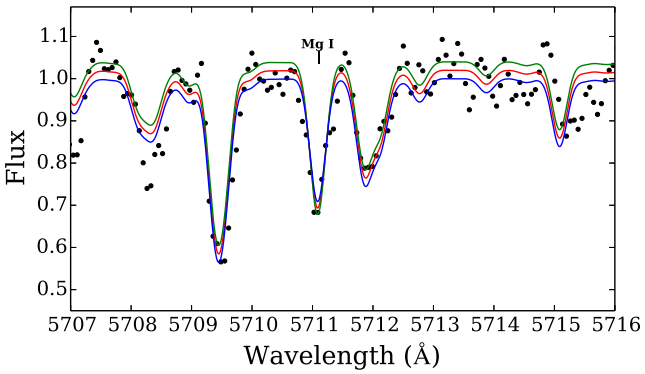

Figure 6. Syntheses of the 5711 Å Mg I line in PA17. The red line shows the best fit, while the green and blue lines are the $\pm 1\sigma$ fits.

The PAndAS cluster [Ca/Fe] ratios are compared to MW and dwarf galaxy field stars in Fig. 7(top) and to MW, M31, and dwarf galaxy GCs in Fig. 7(bottom). Most of the PAndAS GCs are Ca-enhanced, though PA17's [Ca/Fe] is roughly solar. All the PAndAS clusters look very similar to the LMC and Sgr GCs; most of the Fornax clusters are more metal poor than the PAndAS GCs. H10's [Ca/Fe] agrees well with Colucci et al. (2014) and is slightly lower than the average MW and M31 clusters. PA17's low [Ca/Fe] could be understood several ways. As a α-element, low [Ca/Fe] could be indicative of the slow star formation ratios or top-light IMFs seen in dwarf galaxies (e.g. Tinsley 1979; McWilliam et al. 2013) – however, PA17's high [Mg/Fe] ratio suggests that this interpretation is not so simple. Regardless of the cause, PA17's Ca abundance looks most similar to Pal 1, Ter 7, Pal 12, and the LMC field stars and clusters.

4.2.3 *Mg versus Ca*

If Mg and Ca have the same nucleosynthetic site then the [Mg/Ca] ratio should not change with [Fe/H]. In Galactic field stars this is more or less what is observed: [Mg/Ca] is roughly solar except at the lowest metallicities where the dispersion is very high. The dispersion at low metallicities is typically ascribed to inhomogeneous mixing (see e.g. Venn et al. 2012). However, metal-rich dwarf galaxy stars appear to have different [Mg/Ca] ratios from MW stars. In fact, the nucleosynthetic sites of Mg and Ca are *not* the same: Mg is mainly produced during the hydrostatic burning of massive stars (e.g. Woosley & Weaver 1995) while Ca is formed explosively in both Type II and Ia supernovae (e.g. Nomoto et al. 1984; Woosley & Weaver 1995; Maeda et al. 2010). Fig. 8 shows that the metal-rich field stars in the LMC and Fornax have higher [Mg/Ca] ratios than MW stars at the same metallicity – this discrepancy is typically ascribed to the different nucleosynthetic sites of Mg and Ca (e.g. Shetrone et al. 2003; Venn et al. 2004, 2012; Letarte et al. 2010). However, stars in Sgr have low [Mg/Ca] ratios (except possibly for

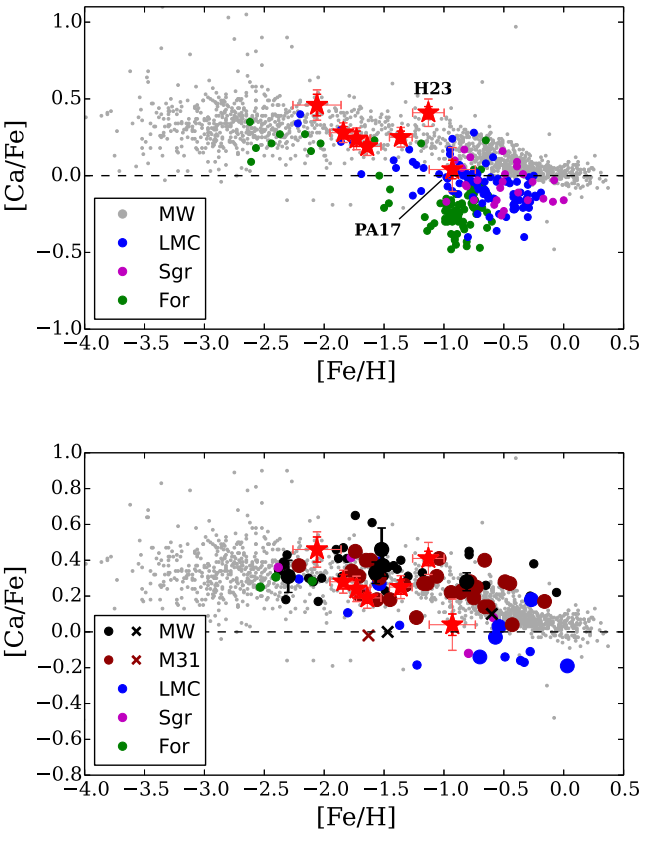

Figure 7. Top: comparisons of PAndAS clusters (red stars) to MW field stars and dwarf galaxy field stars. Points and references are as in Fig. 5(top). Bottom: comparisons of PAndAS clusters (red stars) to MW field stars and GCs from the MW, M31, and various dwarf galaxies. Points and references are as in Fig. 5(bottom).

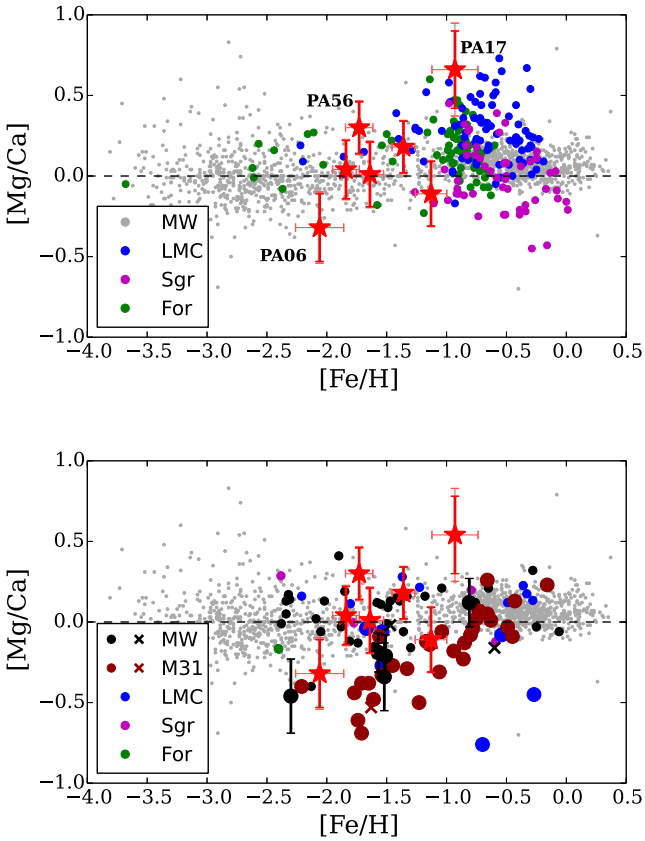

Figure 8. Top: comparisons of PAndAS clusters (red stars) to MW field stars and dwarf galaxy field stars. Points and references are as in Fig. 5(a). Bottom: comparisons of PAndAS clusters (red stars) to MW field stars and GCs from the MW, M31, and various dwarf galaxies. Points and references are as in Fig. 5(b).

stars in the Sgr streams; Monaco et al. 2007); McWilliam et al. (2013) attribute these low ratios to a top-light IMF, where the lack of massive stars means that less Mg is produced than Ca. Most of the PAndAS GCs overlap with Galactic and dwarf galaxy stars; however, PA17's [Mg/Ca] ratio is higher than the Galactic stars, in agreement with the LMC stars.

Again, star-to-star Mg variations could affect the integrated [Mg/Ca] ratios of the metal-poor GCs, complicating comparisons with field stars. However, if the integrated [Mg/Fe] ratios are affected by multiple populations, one might expect the integrated [Mg/Fe] and [Mg/Ca] ratios to be *lower* than the 'primordial' values (because Mg is expected to decrease in the second population). Only PA06 has a lower [Mg/Ca] than the majority of the Galactic stars, in agreement with the integrated [Mg/Ca] of M15, which has known, *strong* star-to-star Mg variations that affect the integrated [Mg/Fe] (Sneden et al. 1997; Sakari et al. 2013). Thus, PA06 seems to be similar to M15, and may host a significant second, Mg-deficient population. The other metal-poor GCs agree well with the Galactic stars and GCs, with the exception of PA56, which has a slightly high [Mg/Ca]. Note that most of the PAndAS GCs have higher [Mg/Ca] ratios than the M31 GCs – again, this is likely because the GCs in the Colucci et al. (2014) sample are more massive than the PAndAS GCs, and therefore may have stronger star-to-star Mg variations.

The GCs more metal rich than [Fe/H] ~ -1.2 are not likely to host significant Mg variations. H10 and H23 have roughly solar [Mg/Ca] ratios, in agreement with the Galactic field stars and clusters (though Colucci et al. 2014 find a lower [Mg/Ca] for H10 because of their lower [Mg/Fe]). PA17 is higher than the Galactic field stars and clusters by $\sim 2\sigma$, in agreement with the LMC and Fornax field stars. This high [Mg/Ca] is driven by the high [Mg/Fe] (determined from spectrum syntheses of the 5711 Å line) and the low [Ca/Fe] (from EWs of four clean lines). Again, the high Mg suggests that PA17 is enriched with the products of the most massive stars, which may be due to IMF effects, stochastic sampling of supernova ejecta, or rotating supernova progenitors (Takahashi et al. 2014 also note that rotating massive stars will not produce as much Ca, compared to non-rotating stars). Despite its agreement with the LMC field stars, PA17 is distinct from the LMC GCs, because the [Mg/Ca] ratios of the metal-rich LMC GCs are not high like the LMC field stars. For the GC with the lowest [Mg/Ca] ratio (NGC 1718), Colucci et al. (2012) suggest an inhomogeneous mixing scenario, where NGC 1718 formed out of material with no contributions from the highest mass stars. However, the three metal-rich, [Mg/Ca]-poor LMC GCs have intermediate ages (1–3 Gyr), and it may not be entirely appropriate to compare these intermediate-age GCs with the older PAndAS GCs. Regardless of the disagreement with the LMC GCs, PA17's high [Mg/Ca] ratio is most similar to the LMC and Fornax field stars.

4.3 Sodium

Sodium abundances are derived from spectrum syntheses of the 6154 and 6160 Å lines, which are all weaker than 100 mÅ in the

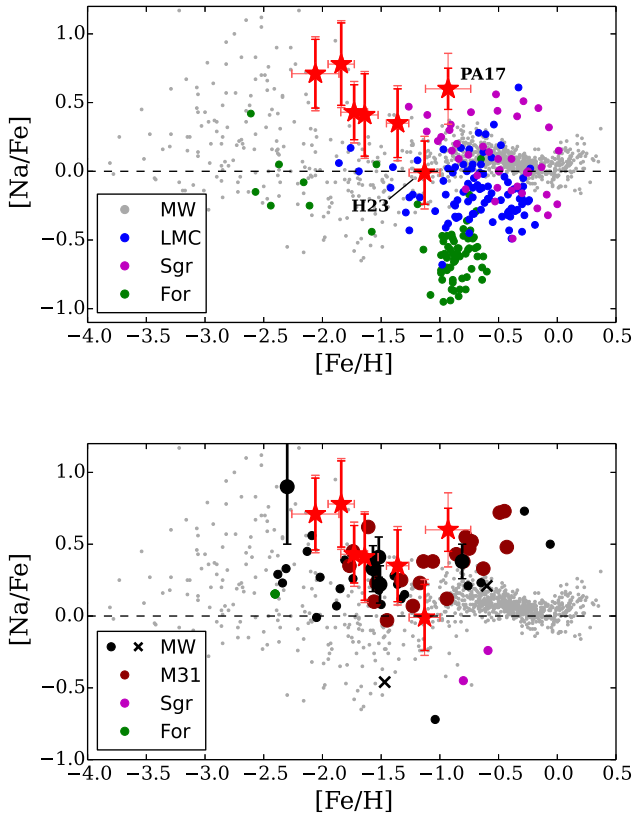

Figure 9. Top: comparisons of PAndAS clusters (red stars) to MW field stars and dwarf galaxy field stars. Points and references are as in Fig. 5(a). Bottom: comparisons of PAndAS clusters (red stars) to MW field stars and GCs from the MW, M31, and various dwarf galaxies. Points and references are as in Fig. 5(b).

PAndAS IL spectra. Sodium lines can be particularly sensitive to NLTE effects; however, the 6154/6160 Å lines are not expected to have significant NLTE corrections (<0.2 dex) at subsolar metallicities and for weak line strengths (e.g. Lind et al. 2011).[14] No corrections were applied to the [Na/Fe] abundances, which are shown in Table 6.

4.3.1 *[Na/Fe]*

Fig. 9 shows comparisons between the PAndAS GCs and the field stars and GCs associated with the various galaxies. Several of the PAndAS GCs have [Na/Fe] ratios that are higher than MW and dwarf galaxy field stars. PA06, PA17, and PA54 all have high [Na/Fe] ratios (>0.6 dex) which places them above the Galactic and dwarf galaxy stars, while the H10, PA53, and PA56 ratios are mildly high (∼0.4 dex). These high values agree well with the IL values of the Galactic and old LMC GCs and with many of the averaged Galactic GCs. In Galactic GCs the [Na/Fe] ratio is affected by star-to-star abundance variations within the clusters, which are often observed as Na/O anticorrelations (see Carretta et al. 2009a). These abundance variations are typically interpreted as arising from two chemically distinct stellar populations within the GCs, which may indicate two separate *generations* of stars (see the review by Gratton, Carretta & Bragaglia 2012). Several Galactic GCs have more centrally concentrated Na-enhanced, O-deficient populations (e.g. M13 and 47 Tuc; Johnson & Pilachowski 2012; Cordero et al. 2014). IL spectra of the central regions (such as the Galactic GCs in Sakari et al. 2013, 2014) will likely be dominated by the second generation (Na-enhanced, O-deficient) populations. It is therefore probable that (like the Galactic GCs) the PAndAS GCs are Na-enhanced because of the presence of multiple populations. It is possible that H23's solar [Na/Fe] is due to the larger coverage of the IL spectrum (see Table 2), which may include light from the less centrally concentrated first generation stars; alternatively, H23 may have more 'primordial' stars. Again, the Colucci et al. (2014) [Na/Fe] ratio for H10 is lower than the one derived here – however, the ratios are derived from only two lines in both cases and are consistent within random and systematic errors.

Thus, the [Na/Fe] ratios indicate that these PAndAS GCs are likely to be 'classical' GCs under the definition of Carretta et al. (2009a, i.e. the GC stars exhibit the Na/O anticorrelation). Note that in this paper only Na abundances are derived for the PAndAS GCs, though O abundances would also be affected by multiple populations. However, the O lines are fairly weak in this wavelength range, and are not easily detectable in such low S/N spectra. Lines in other regions (e.g. the near-infrared) would provide more robust integrated O abundances.

4.3.2 *[Na/Mg]*

Na and Mg are expected to form primarily in massive stars (e.g. Timmes, Woosley & Weaver 1995; Woosley & Weaver 1995); in the absence of multiple population effects, the abundances of Na and Mg are therefore expected to correlate. The MW field stars with [Fe/H] $\gtrsim -2$ show a clear trend of increasing [Na/Mg] with [Fe/H] – Gehren et al. (2006) interpret this as a signature of increasing Na yields with metallicity. However, the metal-poor ($-2 \lesssim$ [Fe/H] $\lesssim -1.2$) Galactic and PAndAS GCs show the opposite trend (see Fig. 10): in PA06 and M15 [Na/Mg] is very high, though [Na/Mg] decreases to subsolar values by [Fe/H] ~ -1.5. The GCs therefore behave in a very different way from the field stars. Again, this is likely to be a result of multiple populations, combined with the metallicity dependency of the Mg/Al anticorrelation (e.g. Carretta et al. 2009a). For these lower mass GCs, at low metallicities the star-to-star Mg variations are likely to be strong in these (fairly bright) GCs, driving the integrated [Mg/Fe] down and [Na/Mg] up. With increasing [Fe/H], the integrated [Mg/Fe] returns to its 'primordial' value, and the [Na/Mg] ratio stabilizes. The [Na/Mg] abundances of the PAndAS GCs therefore also suggest that most of the GCs host multiple populations. Note that the behaviour of the massive M31 clusters (from Colucci et al. 2014) is similar at the metal-poor end, though their [Na/Mg] ratios are higher at the metal-rich end – again, this may be because the massive, metal-rich GCs have stronger Mg variations.

PA17 remains an unusual object, because its similarly high [Na/Fe] and [Mg/Fe] ratios place its [Na/Mg] in agreement with the MW field stars, despite its disagreement in [Mg/Fe]. If PA17's high [Mg/Fe] is caused by increased supernovae ejecta from massive and/or rapidly rotating stars, then [Na/Fe] would also be enhanced; thus, PA17 may have an additional integrated Na enhancement that is caused by contributions from massive stars.

4.4 Nickel

Nickel is expected to form in core-collapse and Type Ia supernovae, along with Fe (Timmes et al. 1995). The [Ni/Fe] ratios

[14] Though note that some of the HRD boxes (see Section 3) can have EWs ∼130 mÅ in the most metal-rich clusters.

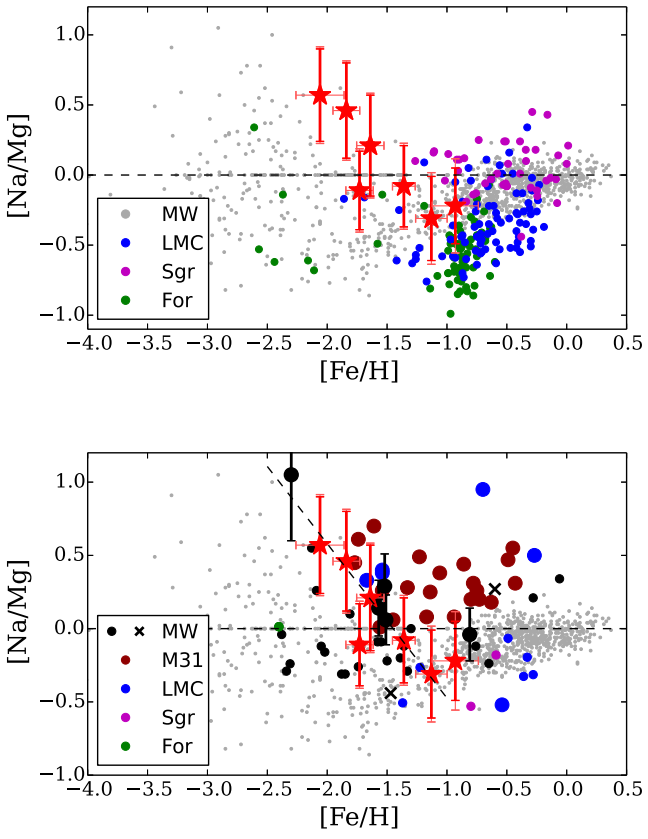

Figure 10. Top: comparisons of PAndAS clusters (red stars) to MW field stars (grey; from the sources in Venn et al. 2004, with supplements from Reddy et al. 2006) and dwarf galaxy field stars. Points and references are as in Fig. 5(a). Bottom: comparisons of PAndAS clusters (red stars) to MW field stars (grey), MW clusters (black circles), inner halo M31 clusters (maroon), and dwarf galaxy GCs. Points and references are as in Fig. 5(b). The dashed line shows the clear linear relationship for the metal-poor GCs ([Fe/H] < -1.2).

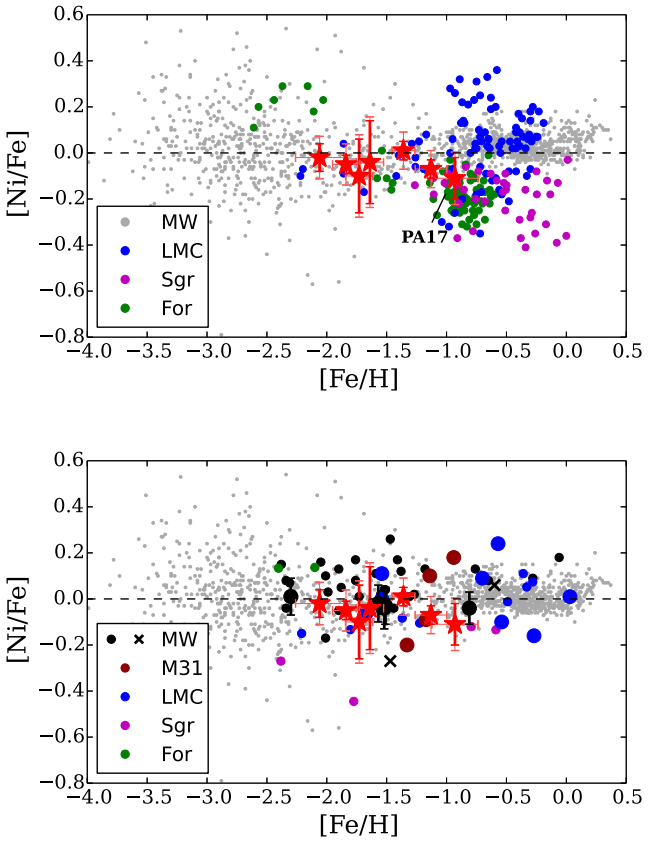

Figure 11. Top: comparisons of Ni abundances in the PAndAS clusters (red stars) to those in MW field stars (grey), dwarf galaxy field stars (coloured points), and the IL abundances of the Galactic clusters (black circles). Points and references are as in Fig. 5(a). Bottom: comparisons of [Ni/Fe] ratios in PAndAS clusters to MW field stars and clusters, Pal 1, and dwarf galaxy clusters. Points and references are as in Fig. 5(b).

were determined with EWs, even though there are few (∼1–7) Ni I lines – however, these lines were carefully checked to ensure that they were clean (i.e. uncontaminated by cosmic rays, sky lines, or noise) and were properly measured. The Ni abundances are given in Table 6 and are compared to field stars and other GCs in Fig. 11. The PAndAS clusters all have [Ni/Fe] ratios that are consistent with MW and dwarf galaxy stars – however, H23 and PA17 both have slightly low Ni abundances, in better agreement with dwarf galaxy stars and GCs. In particular, PA17's [Ni I/Fe I] ratios agree well with the Pal 12 and Ter 7 ratios.

4.5 Neutron capture elements: Ba and Eu

The Ba and Eu abundances are determined through spectrum syntheses. Only two Ba II lines were considered: the 5853 and 6141 Å lines – the 6496 Å line was removed because of possible NLTE effects which lead to abundance overestimates (Mashonkina, Shimanskiĭ & Sakhibullin 2000). No molecular lines are included in these syntheses, since none are identified in those regions in the Arcturus Atlas. The Eu II abundances are determined through syntheses of the 6645 Å line and include CH and CN molecular lines (see Sakari et al. 2013); these syntheses are shown in Fig. 12. HFS and isotopic components were included for the Ba II and Eu II lines, as described in Section 2.3.

Sakari et al. (2014) demonstrated that the [Ba/Eu] ratio is often more stable than the individual [Ba/Fe] and [Eu/Fe] ratios to uncertainties in the underlying population. Comparisons of [Ba/Eu] ratios are shown in Fig. 13, and illustrate that metal-rich dwarf galaxy stars have higher [Ba/Eu] ratios than MW field stars. PA06 and PA54 only have upper limits on the Eu abundance, which translates into a lower limit in [Ba/Eu]. The estimated r-process-only ratio (from Burris et al. 2000) is also indicated in Fig. 13. The PAndAS GCs agree with the MW field stars and GCs, with the exception of PA17 and PA56. PA56 has a low [Ba/Eu], much like M15. Both Ba and Eu have been known to vary within some of the most massive metal-poor GCs[15] (such as M15; see e.g. Sneden et al. 1997; Roederer 2011); neutron star mergers have been suggested as the origin of these star-to-star heavy element variations (e.g. Tsujimoto & Shigeyama 2014). PA56's IL abundances may also be affected by the presence of heavy element dispersions with the GCs. Table 6 shows that PA56 has a moderate Ba abundance and a high Eu abundance, which leads to a [Ba/Eu] that is below the r-process-only estimate; this indicates that PA56 may host stars with a significant heavy element dispersion.

PA17's high [Ba/Eu] is in agreement with the Galactic GCs within its 1σ errors, though it agrees best with the dwarf galaxy stars and

[15] Though note that not all massive GCs show heavy element variations, e.g. M92 (Cohen 2011).

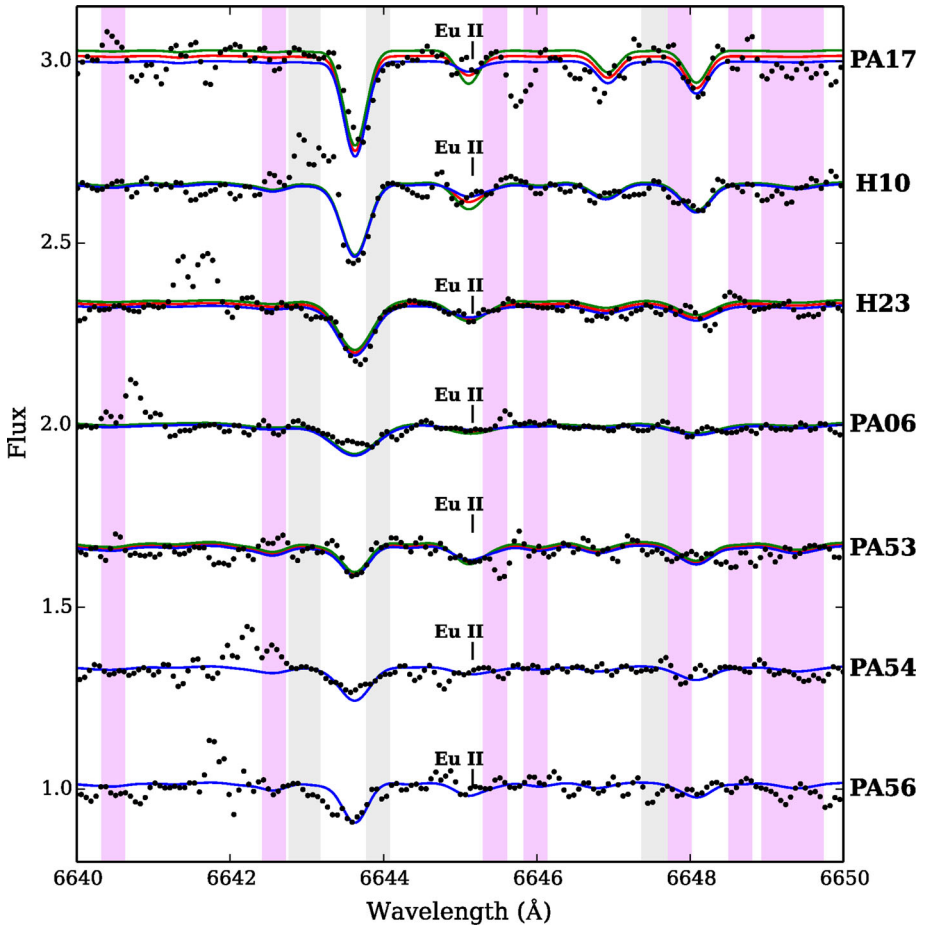

Figure 12. Syntheses of the 6645 Å Eu II line. Grey regions show areas with uncertain HFS, while purple regions indicate uncertain molecular features. The red lines show the best fit, while the green and blue lines show $\pm 1\sigma$ uncertainties. PA06 and PA56 have only upper limits for the Eu II abundance.

GCs, Pal 1, and Pal 12. The high [Ba/Eu] ratios in dwarf galaxies are typically interpreted as an excess of s-process over r-process elements. Its moderately high [Ba/Eu] ratio indicates that PA17 has received chemical contributions from AGB stars.

[Eu/α] is another popular chemical tagging indicator since dwarf galaxy stars and GCs have higher [Eu/α] ratios than MW stars and GCs at a given [Fe/H] – this has been interpreted as a sign of an additional r-process site (e.g. Letarte et al. 2010) or a top-light IMF (e.g. McWilliam et al. 2013). Figs 14(top) and (bottom) show the [Eu/Ca] ratios (which serve as [Eu/α] indicators) in different environments. Again, only upper limits are available for PA06 and PA54. In general the clusters are in agreement with the MW and dwarf galaxy field stars and GCs, with the exception of PA56, which has a high [Eu/Ca], similar to M15 – again, this is likely a signature of star-to-star Eu variations.

5 DISCUSSION

The detailed abundances of stars are dictated by the chemical composition of the interstellar medium in their host galaxy. Chemical comparisons between the PAndAS GCs and the field stars and GCs associated with other galaxies therefore provide clues about the nature of a GC's birth environment, such as whether a cluster formed in a massive galaxy or a dwarf galaxy. Chemical comparisons can also determine if the GCs are chemically similar to *particular* galaxies, streams, or other GCs. If these GCs originated in dwarf galaxies, the abundances in this paper can therefore be used to infer the nature of the dwarfs that are currently being accreted into M31's outer halo.

5.1 Individual clusters: a summary

5.1.1 PAndAS clusters with [Fe/H] >−1.5

The more metal-rich clusters all have higher metallicities than expected given their large projected distances from the centre of M31. However, each GC has a unique chemical signature.

PA17. Without *HST* photometry, PA17's abundances are more uncertain than the other GCs; however, the high [Na/Fe] ratio suggests that PA17 is a 'classical' GC (under the Carretta et al. 2009a definition) with signs of a Na spread (and therefore probably an O spread as well). PA17 is the most metal rich of the target clusters, at [Fe/H] ~ -0.9. Despite the lack of *HST* photometry, systematic errors in [Fe/H] are likely to be $\lesssim$0.2 dex. PA17's metallicity alone indicates that it formed in a fairly massive galaxy – its unusual location far away in the outer halo ($R_{\rm proj} \sim 54$ kpc; Huxor et al. 2014) suggests that it formed in a dwarf galaxy like the LMC or Sgr.

PA17's low [Ca/Fe] and high [Mg/Ca] and [Ba/Eu] ratios indicate that PA17 is more *chemically* similar to the LMC stars and clusters than to those associated with the MW (and presumably to those in M31), even when systematic offsets are considered. As discussed earlier, the [α/Fe] and [Ba/Eu] ratios indicate whether a cluster formed in an environment enriched by Type Ia supernova

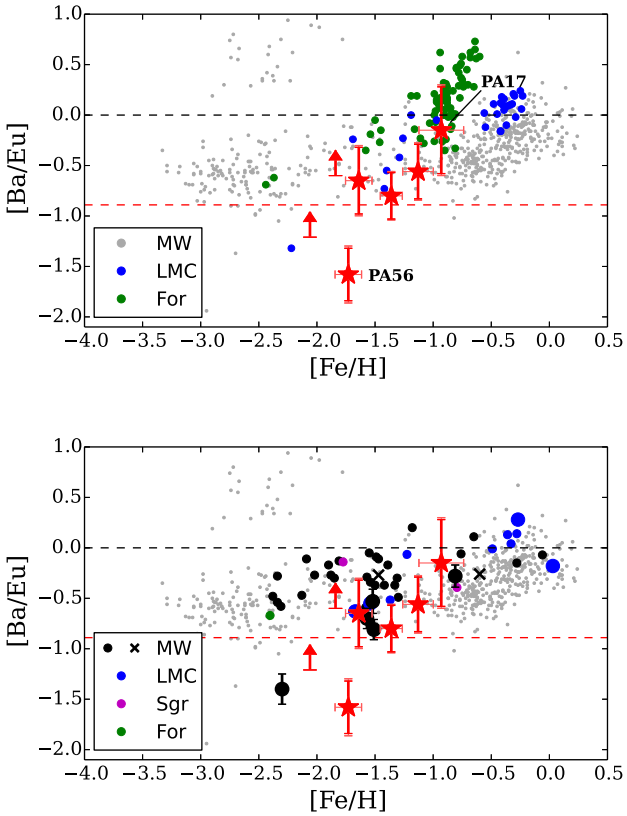

Figure 13. Top: comparisons of PAndAS clusters (red stars) to MW field stars and dwarf galaxy field stars. Points and references are as in Fig. 5(a). The dashed red line shows the r-process-only limit from Burris et al. (2000). Bottom: comparisons of PAndAS clusters (red stars) to MW field stars and GCs from the MW, M31, and various dwarf galaxies. Points and references are as in Fig. 7(b).

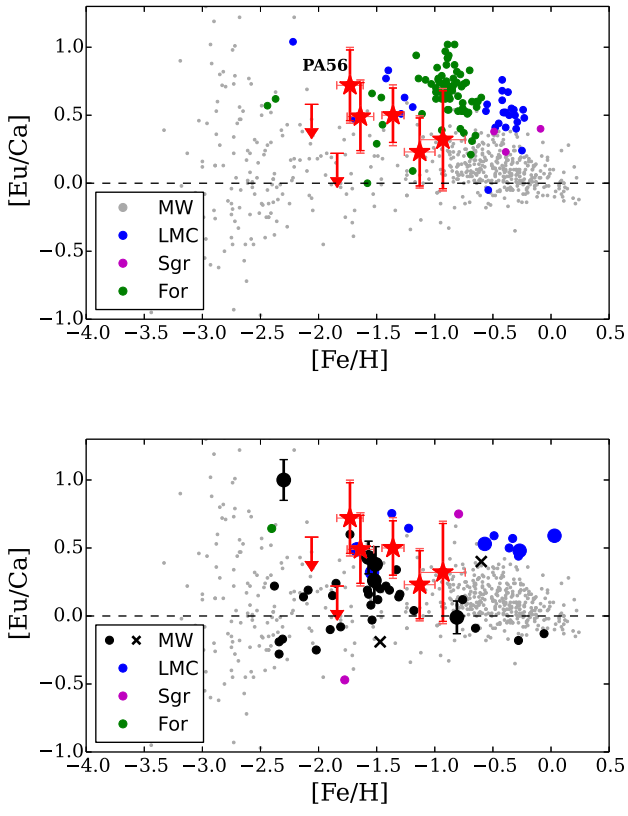

Figure 14. Top: comparisons of PAndAS clusters (red stars) to MW field stars and dwarf galaxy field stars. Points and references are as in Fig. 5(a). Bottom: comparisons of PAndAS clusters (red stars) to MW field stars and GCs from the MW, M31, and various dwarf galaxies. Points and references are as in Fig. 7.

and AGB star products. Combined with its metallicity, PA17's detailed chemical abundance ratios therefore indicate that it formed in a galaxy which had sufficient mass to have a fairly high star formation rate or to populate the high-mass end of the IMF. However, its high [Mg/Fe] (and possibly its high [Na/Fe]) indicates that PA17 may have been enriched in ejecta from the most massive stars. As discussed in Sections 4.2 and 4.3 this suggests that PA17's progenitor galaxy had more massive stars than a typical dwarf (i.e. it had a top-heavy IMF), was enriched by supernova ejecta from a rapidly rotating massive star, and/or was uniquely enriched from the products of a supernova due to inhomogeneous mixing in the host galaxy.

Ultimately, PA17's integrated abundances are chemically distinct from those of the metal-rich Galactic GC 47 Tuc, and are similar to Pal 1, the intermediate-age LMC clusters, and the accreted Sgr clusters Pal 12 and Ter 7.

H10 and H23. H10 and H23 are the third and second most metal-rich GCs in the sample of PAndAS GCs, respectively. Based on the same arguments as for PA17, this indicates that the clusters likely originated in LMC- or Sgr-like dwarf galaxies. Unlike PA17, H23's chemical abundance ratios are indistinguishable from MW field stars and clusters and M31 GCs at the same [Fe/H]. H10's [Ca/Fe] is mildly low while its [Mg/Ca] and [Eu/Ca] ratios are mildly high – this [Ca/Fe] ratio could indicate that H10 formed in a dwarf galaxy with a knee in the [Ca/Fe] versus [Fe/H] relationship near [Fe/H] ~ -1.5, similar to LMC intermediate-aged clusters.

5.1.2 *PAndAS clusters with [Fe/H] <−1.5*

It is more difficult to tag metal-poor GCs ([Fe/H] $\lesssim -1.5$) with chemical abundances, since the chemistries of metal-poor stars in dwarf galaxies and massive galaxies are not always significantly different. The analysis is further complicated by potential star-to-star Na, Mg, Ba, and Eu variations within the GCs.

PA53 and PA56. These clusters are fairly close to each other in projection, and have very similar radial velocities and metallicities; it is therefore possible that these clusters are physically associated with one another and were accreted from the same dwarf. Their discrepant Mg, Ba, and Eu ratios do not preclude the possibility that they are related, as the integrated abundances may be affected by star-to-star variations within the clusters. Both GCs are slightly enhanced in Na (with [Na/Fe]$\sim$0.4), which is likely a signature of the Na/O anticorrelation. PA56 also has a very low [Ba/Eu] (below the r-process-only yields), similar to M15, which supports the idea that it may have star-to-star heavy element variations. Both clusters are metal poor ([Fe/H] ~ -1.7) and have [Ca/Fe] ratios slightly lower than the MW field stars, similar to the Fornax field stars.

PA54. Although PA54 is extremely close to PA53 in projection, their discrepant radial velocities imply that these clusters are not likely to be associated, nor is PA54 likely to be associated with PA56. However, PA54 has very similar abundance ratios as PA53 and PA56, even with only upper limits on [Eu/Fe]. This indicates that PA54 may have formed in similar conditions.

PA06. PA06 is the most metal-poor PAndAS GC in this analysis, though it is still more metal rich than the Galactic GC M15. Again,

PA06's high [Na/Fe] indicates the presence of a Na/O anticorrelation – additionally, its low [Mg/Fe] hints at a Mg/Al anticorrelation. PA06 is similar to the metal-poor GCs in the MW (particularly M15) and in the dwarf galaxies: it is metal poor and α-enhanced. The weakness of its spectral lines means that only an upper limit can be obtained for Eu II.

5.2 Comparisons with M31 halo stars

The presence of streams in the metal-poor density map of M31's outer halo (see Fig. 1) implies that some metal-poor (i.e. low-mass) dwarf galaxies are currently being accreted. The chemical ratios of PA06, PA53, PA54, and PA56 are all consistent with an accretion origin in at least one metal-poor dwarf galaxy. None of these GCs has been associated with streams based on their positions. Given their lack of association with any streams, if PA06 and PA54 were accreted from dwarf satellites they may be remnants of ancient accretion events; Ibata et al. (2014) estimate that ∼58 per cent of the metal-poor halo ([Fe/H] $\lesssim -1.7$) resides in a 'smooth' component, which may include these GCs.

Recall that PA53 and PA56 are located near the eastern cloud. Their similar kinematics and chemical compositions hint that PA53 and PA56 are associated with each other – however, the numbers of stars around the clusters (Mackey et al., in preparation), their metallicities, and their detailed chemical abundances indicate that PA53 and PA56 were also likely associated with the dwarf galaxy that created the Eastern Cloud. In this case, the Eastern Cloud must turn back towards M31, encompassing PA53. This further suggests that the Eastern Cloud's progenitor must have been massive enough to form GCs, though not sufficiently massive to produce a significant metal-rich stellar population.

The presence of the metal-rich Giant Stellar Stream (GSS), the associated H I gas, the outer halo stellar mass, and the number of metal-rich GCs in the outer halo indicate that M31 likely experienced a minor merger with a Sgr or LMC-mass galaxy (e.g. Fardal et al. 2013; Lewis et al. 2013; Bate et al. 2014). Ibata et al. (2014) find that 86 per cent of the most metal-rich stars ([Fe/H] $\gtrsim -0.5$) in the outer halo are associated with substructure from an accreted companion. Though this number decreases with metallicity, the fraction of accreted stars still remains high: 78 per cent of the stars in PA17's metallicity bin ($-1.1 \lesssim$ [Fe/H] $\lesssim -0.5$) are expected to be associated with coherent, accreted structures, while 58 per cent of the stars in H10 and H23's metallicity bin ($-1.7 \lesssim$ [Fe/H] $\lesssim -1.1$) are expected to be in streams. It is therefore likely that these comparatively metal-rich GCs were associated with dwarf satellites. H23 has been tentatively linked to a stream near the GSS (Stream D; see Veljanoski et al. 2014) based on its position, though its kinematics indicate that such an association is unlikely; neither H10 nor PA17 has been linked to any visible stellar streams, though *HST* imaging of fields around H10 and H23 reveals extremely metal-rich populations of field stars, suggesting that the GCs may be located on low surface brightness streams (Richardson et al. 2009).

H10 is located near the SW cloud, an overdensity of stars to the south-west of M31.[16] With photometry, Bate et al. (2014) estimate that the cloud hosts a metal-rich population ([Fe/H] ~ -1.3), and that the progenitor galaxy was a fairly bright dwarf ($M_V \sim -12$, which is slightly fainter than Fornax and Sgr). Three GCs (PA7, PA8, and PA14) appear to be kinematically associated with each other and with the SW Cloud (Mackey et al. 2013, 2014; Bate et al. 2014; Veljanoski et al. 2014). The SW Cloud does extend to the south-east, and H10 lies at the end of this extension (see fig. 2 in Bate et al. 2014). H10's radial velocity (-352 km s^{-1}) agrees with the stream's radial velocity and that of the GCs, and even agrees with the velocity gradient noted by Bate et al. (where the northernmost GC, PA7, is moving towards the MW faster than PA8 and PA17). Furthermore, H10's [Fe/H] ~ -1.4 agrees very well with the cloud and its GCs, and its detailed abundances support the idea that it could have originated in a dwarf galaxy with the mass of Fornax or Sgr. Thus, it is likely that H10 is associated with PA7, PA8, PA14, and the SW Cloud.

As mentioned above, H23 has been spatially associated with Stream D based on its position, though its velocity disagrees with the other GCs in the stream. Its metallicity, [Fe/H] $= -1.1$, now further suggests that H23 is not likely to be associated with that stream, since Stream D is primarily composed of metal-poor stars with [Fe/H] < -1.1 (Ibata et al. 2014). It is more likely that H23 came from the progenitor of the GSS, along with PA17. Fardal et al. (2013) perform *N*-body simulations to reproduce the GSS and other stellar debris. These simulations indicate that a massive progenitor was accreted during multiple orbits, culminating in a recent final accretion (∼760 Myr ago). Many of the metal-rich PAndAS GCs might have been stripped early on, and may no longer be associated with any bright, coherent substructure. Given their metallicities and other chemical abundances, it is possible that H23 and PA17 both formed in the GSS progenitor. If H23 and PA17 were born in the same dwarf galaxy, their [Ca/Fe] ratios clearly imply a 'knee' at [Fe/H] ~ -1.1 to -1.3, similar to the LMC stars and clusters.

6 CONCLUSIONS

This paper has presented integrated Fe, Na, Mg, Ca, Ti, Ni, Ba, and Eu abundances of seven outer halo M31 GCs, five of which were discovered in the PAndAS. These detailed IL chemical analyses of PAndAS clusters have identified GCs in an extragalactic system that may have been accreted from dwarf galaxies. Detailed investigations of the chemical abundance ratios of individual targets such as this are only possible with high-resolution spectroscopy.

The PAndAS cluster abundances suggest that these outer halo M31 GCs may have been accreted from multiple dwarf galaxies:

(i) The metal-rich GC PA17 is chemically more similar to the LMC stars and clusters than to MW field stars and clusters, suggesting that it originated in an LMC-like dwarf galaxy. H23's abundances are indistinguishable from MW field stars and clusters, though its metallicity and location suggest it may have originated in a massive dwarf galaxy. PA17 and H23 may have been accreted along with the progenitor of the metal-rich GSS.

(ii) The intermediate-metallicity GC H10 has a location, metallicity, and radial velocity that agree well with the SW Cloud and its GCs, which may have originated in a Sgr- or Fornax-sized progenitor (Bate et al. 2014). H10's chemical abundance ratios support the suggestion that it may have formed in a dwarf galaxy.

(iii) PA53, PA54, and PA56 have abundances and metallicities that are more typical of an intermediate-mass dwarf galaxy like Fornax. This suggests that they are currently being accreted from at least one metal-poor dwarf galaxy and could be associated with one or more of the coherent, metal-poor streams observed in PAndAS.

[16] Note that though PA17's proximity to PA14 hints at an association with the SW Cloud, its drastically different radial velocity (-260 km s^{-1}) from PA14 (-363 km s^{-1}; Veljanoski et al. 2014) and high [Fe/H] (-0.93 compared to -1.30; Mackey et al. 2013) make it unlikely that PA17 was associated with the SW Cloud progenitor.

Based on their chemistries and radial velocities PA53 and PA56 could be associated and are likely to have been accreted from the dwarf galaxy that created the Eastern Cloud. Despite its proximity in projection, it is unlikely that PA54 is associated with either PA53 or PA56.

(iv) PA06's metallicity makes it a difficult target for chemical tagging analyses, since the chemistries between dwarf and massive galaxies have likely not had sufficient time to diverge at [Fe/H] ~ -2. Several of its integrated abundances do not agree with MW or dwarf galaxy stars, suggesting that strong star-to-star chemical variations are present in the cluster.

Thus, this chemical tagging analysis is consistent with the observation that M31's outer halo GC system is being built up by accretion of dwarf satellites. In addition, this detailed abundance analysis provides additional information on the nature of these progenitor systems that is, at present, very difficult to obtain from the field populations.

ACKNOWLEDGEMENTS

The authors thank Don VandenBerg for his suggestion to investigate the RGB slope calibration, for providing the isochrones in *HST* magnitudes, and for all his comments. The authors also thank Judy Cohen for providing a helpful referee report that contributed to this analysis, Andy McWilliam for his help and support, and George Wallerstein for reading the manuscript. CMS acknowledges funding from the Natural Sciences and Engineering Research Council (NSERC), Canada, via the Vanier CGS program. KAV acknowledges funding through the NSERC Discovery Grants program. DM (for Dougal Mackey) is grateful for support by an Australian Research Fellowship (Grant DP1093431) from the Australian Research Council. The Hobby–Eberly Telescope (HET) is a joint project of the University of Texas at Austin, the Pennsylvania State University, Stanford University, Ludwig-Maximilians-Universität München, and Georg-August-Universität Göttingen. The HET is named in honour of its principal benefactors, William P. Hobby and Robert E. Eberly. The authors wish to thank the night operations staff of the HET for their assistance and expertise with these unusual observations. This work has made use of BaSTI web tools.

REFERENCES

Anderson J. et al., 2008, AJ, 135, 2055
Asplund M., Grevesse N., Sauval J. A., Scott P., 2009, ARA&A, 47, 481
Bate N. F. et al., 2014, MNRAS, 437, 3362
Bernard E. J. et al., 2015, MNRAS, 446, 2789
Burris D. L., Pilachowski C. A., Armandroff T. E., Sneden C., Cowan J. J., Roe H., 2000, ApJ, 544, 302
Caldwell N., Schiavon R., Morrison H., Rose J. A., Harding P., 2011, AJ, 141, 18
Cameron S., 2009, PhD thesis, Univ. Michigan, Michigan
Carretta E., Bragaglia A., Gratton R., Lucatello S., 2009a, A&A, 505, 139
Carretta E., Bragaglia A., Gratton R., D'Orazi V., Lucatello S., 2009b, A&A, 508, 695
Carretta E. et al., 2010, A&A, 520, A95
Casagrande L., VandenBerg D. A., 2014, MNRAS, 444, 392
Castelli F., Kurucz R. L., 2004, in Piskunov N., Weiss W. W., Gray D. F., eds, Proc. IAU Symp. 210, Modelling of Stellar Atmospheres. Astron. Soc. Pac., San Francisco, p. A20
Chou M.-Y., Cunha K., Majewski S. R., Smith V. V., Patterson R. J., Martnez-Delgado D., Geisler D., 2010, ApJ, 708, 1290
Cohen J., 2004, AJ, 127, 1545
Cohen J. G., 2011, ApJ, 740, L38
Cohen J. G., Melendez J., 2005, AJ, 129, 303
Colucci J. E., Bernstein R. A., 2011, EAS Publ. Ser., 48, 275
Colucci J. E., Bernstein R. A., Cameron S., McWilliam A., Cohen J. G., 2009, ApJ, 704, 385
Colucci J. E., Bernstein R. A., Cameron S. A., McWilliam A., 2011, ApJ, 735, 55
Colucci J. E., Bernstein R. A., Cameron S. A., McWilliam A., 2012, ApJ, 746, 29
Colucci J. E., Duran M. F., Bernstein R. A., McWilliam A., 2013, ApJ, 773, 36
Colucci J. E., Bernstein R. A., Cohen J., 2014, ApJ, 797, 116
Cordero M. J., Pilachowski C. A., Johnson C. I., McDonald I., Zijlstra A. A., Simmerer J., 2014, ApJ, 780, 94
Cordier D., Pietrinferni A., Cassisi S., Salaris M., 2007, AJ, 133, 468
Fardal M. A. et al., 2013, MNRAS, 434, 2779
Ferguson A. M. N., Irwin M. J., Ibata R. A., Lewis G. F., Tanvir N. R., 2002, AJ, 124, 1452
Freeman K., Bland-Hawthorn J., 2002, ARA&A, 40, 487
Gehren T., Shi J. R., Zhang H. W., Zhao G., Korn A. J., 2006, A&A, 451, 1065
Gratton R. G., Carretta E., Bragaglia A., 2012, A&AR, 20, 50
Hanuschik R. W., 2003, A&A, 407, 1157
Hinkle K., Wallace L., Livingston W., Ayres T., Harmer D., Valenti J., 2003, in Brown A., Harper G. M., Ayres T. R., eds, The Future of Cool-Star Astrophysics: 12th Cambridge Workshop on Cool Stars, Stellar Systems, and the Sun. University of Colorado, Boulder, p. 851
Huxor A. P., Tanvir N. R., Ferguson A. M. N., Irwin M. J., Ibata R., Bridges T., Lewis G. F., 2008, MNRAS, 385, 1989
Huxor A. P. et al., 2014, MNRAS, 442, 2165
Ibata R., Irwin M., Lewis G., Ferguson A. M. N., Tanvir N., 2001, Nature, 412, 49
Ibata R., Martin N. F., Irwin M., Chapman S., Ferguson A. M. N., Lewis G. F., McConnachie A. W., 2007, ApJ, 671, 1591
Ibata R. A. et al., 2013, Nature, 493, 62
Ibata R. A. et al., 2014, ApJ, 780, 128
Johnson C. I., Pilachowski C. A., 2012, ApJ, 754, L38
Johnson J. A., Ivans I. I., Stetson P. B., 2006, ApJ, 640, 801
Johnston K. V., Bullock J. S., Sharma S., Font A., Robertson B. E., Leitner S. N., 2008, ApJ, 689, 936
Kroupa P., 2002, Science, 295, 82
Kupka F., Ryabchikova T. A., Piskunov N. E., Stempels H. C., Weiss W. W., 2000, Balt. Astron., 9, 590
Kurucz R. L., 2005, Mem. Soc. Astron. Ital., 8, 189
Lawler J. E., Bonvallet G., Sneden C., 2001a, ApJ, 556, 452
Lawler J. E., Wickliffe M. E., den Hartog E. A., Sneden C., 2001b, ApJ, 563, 1075
Lee H.-C., Worthey G., 2005, ApJS, 160, 176
Letarte B., Hill V., Jablonka P., Tolstoy E., François P., Meylan G., 2006, A&A, 453, 547
Letarte B. et al., 2010, A&A, 523, A17
Lewis G. F. et al., 2013, ApJ, 763, 4
Lind K., Asplund M., Barklem P. S., Belyaev A. K., 2011, A&A, 528, 103
McConnachie A. W. et al., 2009, Nature, 461, 66
Mackey A. D. et al., 2007, ApJ, 655, L85
Mackey A. D. et al., 2010, ApJ, 717, L11
Mackey A. D. et al., 2013, MNRAS, 429, 281
Mackey A. D. et al., 2014, MNRAS, 445, L89
McWilliam A., 1998, AJ, 115, 1640
McWilliam A., Bernstein R., 2008, ApJ, 684, 326
McWilliam A., Preston G. W., Sneden C., Searle L., 1995, AJ, 109, 2757
McWilliam A., Wallerstein G., Mottini M., 2013, ApJ, 778, 149
Maeda K., Röpke F. K., Fink M., Hillebrandt W., Travaglio C., Thielemann F.-K., 2010, ApJ, 712, 624
Mashonkina L. I., Shimanskiĭ V. V., Sakhibullin N. A., 2000, Astron. Rep., 44, 790

Mitschang A. W., De Silva G., Zucker D. B., Anguiano B., Bensby T., Feltzing S., 2014, MNRAS, 438, 2753
Monaco L., Bellazzini M., Bonifacio P., Buzzoni A., Ferraro F. R., Marconi G., Sbordone L., Zaggia S., 2007, A&A, 464, 201
Mottini M., Wallerstein G., McWilliam A., 2008, AJ, 136, 614
Mucciarelli A., Carretta E., Origlia L., Ferraro F. R., 2008, AJ, 136, 375
Nissen P. E., Schuster W. J., 2010, A&A, 511, L10
Nomoto K., Thielemann F. K., Yokoi K., 1984, ApJ, 286, 644
Peng E. et al., 2006, ApJ, 639, 95
Pietrinferni A., Cassisi S., Salaris M., Castelli F., 2004, ApJ, 612, 168
Pompéia L. et al., 2008, A&A, 480, 379
Pritzl B. J., Venn K. A., Irwin M., 2005, AJ, 130, 2140
Puzia T. H., Sharina M. E., 2008, ApJ, 674, 909
Puzia T. H., Kissler-Patig M., Goudfrooij P., 2006, ApJ, 648, 383
Ramsey L. W. et al., 1998, Proc. SPIE, 3352, 34
Reddy B. E., Lambert D. L., Prieto C. A., 2006, MNRAS, 367, 1329
Richardson J. C. et al., 2009, MNRAS, 396, 1842
Roederer I. U., 2011, ApJ, 732, L17
Sakari C. M., Venn K. A., Irwin M., Aoki W., Arimoto N., Dotter A., 2011, ApJ, 740, 106
Sakari C. M., Shetrone M., Venn K., McWilliam A., Dotter A., 2013, MNRAS, 434, 358
Sakari C. M., Venn K., Shetrone M., Dotter A., Mackey D., 2014, MNRAS, 443, 2285
Salaris M., Chieffi A., Straniero O., 1993, ApJ, 414, 580
Sarajedini A., 1994, AJ, 107, 618
Sarajedini A. et al., 2007, AJ, 133, 1658
Sbordone L., Bonifacio P., Marconi G., Buonanno R., Zaggia S., 2005, A&A, 437, 905
Sbordone L., Bonifacio P., Buonanno R., Marconi G., Monaco L., Zaggia S., 2007, A&A, 465, 815
Schiavon R. P., Faber S. M., Castilho B. V., Rose J. A., 2002, ApJ, 580, 850
Shetrone M., Venn K., Tolstory E., Primas F., Hill V., Kaufer A., 2003, AJ, 125, 684
Shetrone M. D. et al., 2007, PASP, 119, 556
Sneden C., 1973, ApJ, 184, 839
Sneden C., Kraft R. P., Shetrone M. D., Smith G. H., Langer G. E., Prosser C. F., 1997, AJ, 114, 1964
Sneden C., Kraft R. P., Guhathakurta P., Peterson R. C., Fulbright J., 2004, AJ, 127, 2162
Stetson P. B., Pancino E., 2008, PASP, 120, 1332
Tafelmeyer M. et al., 2010, A&A, 524, A58
Takahashi K., Umeda H., Yoshida T., 2014, ApJ, 794, 40
Tanvir N. R. et al., 2012, MNRAS, 422, 162
Timmes F. X., Woosley S. E., Weaver T. A., 1995, ApJS, 98, 617
Ting Y. S., Freeman K. C., Kobayashi C., De Silva G. M., Bland-Hawthorn J., 2012, MNRAS, 421, 1231
Tinsley B. M., 1979, ApJ, 229, 1046
Tolstoy E., Hill V., Tosi M., 2009, ARA&A, 47, 371
Tsujimoto T., Shigeyama T., 2014, ApJ, 795, L18
Tull R. G., 1998, Proc. SPIE, 3355, 387
VandenBerg D. A., Bergbusch P. A., Dotter A., Ferguson J. W., Michaud G., Richer J., Proffitt C. R., 2012, ApJ, 755, 15
VandenBerg D. A., Brogaard K., Leaman R., Casagrande L., 2013, ApJ, 775, 134
VandenBerg D. A., Bergbusch P. A., Ferguson J. W., Edvardsson B., 2014, ApJ, 794, 23
Vargas L. C., Gilbert K. M., Geha M. C., Tollerud E. J., Kirby E. N., Guhathakurta P., 2014, ApJ, 797, L2
Veljanoski J. et al., 2013, ApJ, 768, L33
Veljanoski J. et al., 2014, MNRAS, 442, 2929
Venn K. A., Irwin M., Shetrone M. D., Tout C. A., Hill V., Tolstoy E., 2004, AJ, 128, 1177
Venn K. A. et al., 2012, ApJ, 751, 102
Villanova S., Geisler D., Carraro G., Moni Bidin C., Muñoz C., 2013, ApJ, 778, 186
Woosley S. E., Weaver T. A., 1995, ApJS, 101, 181

Table A1. Galactic GC RGB slopes.

Cluster	[Fe/H]	RGB slope
M92	-2.35 ± 0.05	-11.429 ± 1.172
M15	-2.33 ± 0.05	-11.765 ± 1.238
M53	-1.93 ± 0.05	-10.929 ± 1.077
NGC 5286	-1.70 ± 0.05	-10.870 ± 1.066
M2	-1.66 ± 0.05	-9.346 ± 0.799
M13	-1.58 ± 0.05	-9.217 ± 0.778
M3	-1.50 ± 0.05	-9.091 ± 0.758
M5	-1.33 ± 0.05	-8.299 ± 1.181
NGC 1261	-1.27 ± 0.05	-7.937 ± 1.087
NGC 1851	-1.18 ± 0.05	-7.491 ± 0.976
NGC 6362	-1.07 ± 0.05	-6.557 ± 0.760
47 Tuc	-0.76 ± 0.05	-3.766 ± 1.031
NGC 6652	-0.76 ± 0.05	-4.090 ± 1.187
M69	-0.59 ± 0.05	-3.883 ± 1.086
NGC 5927	-0.29 ± 0.05	-7.491 ± 0.595

References: cluster [Fe/H] ratios are from Carretta et al. (2009b).

APPENDIX A: RGB SLOPE VERSUS METALLICITY: A CALIBRATION WITH GALACTIC GLOBULAR CLUSTER OPTICAL CMDS

It is well established that the slope of a cluster's RGB is correlated with cluster metallicity (e.g. Sarajedini 1994). This appendix discusses the calibration of RGB slope versus [Fe/H], utilizing high-quality *HST* CMDs of Galactic GCs from the ACS Survey of Galactic Globular Clusters (Sarajedini et al. 2007; Anderson et al. 2008).[17] For this calibration 15 Galactic GCs with high-quality CMDs and well-populated RGBs that span a wide range in [Fe/H] were selected; priority was given to clusters with low foreground reddening. Using the original *F606W* and *F814W HST* magnitudes, the distance moduli from VandenBerg et al. (2013) were used to overplot clusters, and distance moduli and reddening values were adjusted so that cluster HBs overlapped. The average RGB colours were then determined at two magnitudes ($M_V = 0$ and -2), and RGB slopes were calculated. These points are shown in Fig. A1, while the slopes are listed in Table A1.

Uncertainties in RGB slope were estimated based on the uncertainties in colour at the two magnitudes. The metal-poor clusters have small uncertainties in RGB colour, though this translates into large uncertainties in slope because the RGBs are steeper. The metal-rich clusters have very uncertain RGB colours, but because the RGBs are flatter the uncertainty in slope is much lower. Note that at higher [Fe/H] ($\gtrsim -0.7$) a linear fit to the RGB is no longer a good approximation to the actual shape of the RGB – thus, this calibration is likely to break down at the metal-rich end.

For each cluster the [Fe/H] ratios from Carretta et al. (2009b) were adopted; [Fe/H] uncertainties of 0.05 dex were assumed. Fig. A2 shows the relationship between RGB slope and cluster [Fe/H]. The linear least-squares fit to the points is shown with the solid line, while the dashed lines show the uncertainty in the fit. The trend is clear: metal-poor GCs have steeper RGBs than more metal-rich GCs. Non-standard chemical abundance mixtures (in e.g. C, N, O, or α-elements like Mg or Si) can affect the shape of the RGB (e.g. Salaris, Chieffi & Straniero 1993; VandenBerg et al. 2012),

[17] http://www.astro.ufl.edu/~ata/public_hstgc/

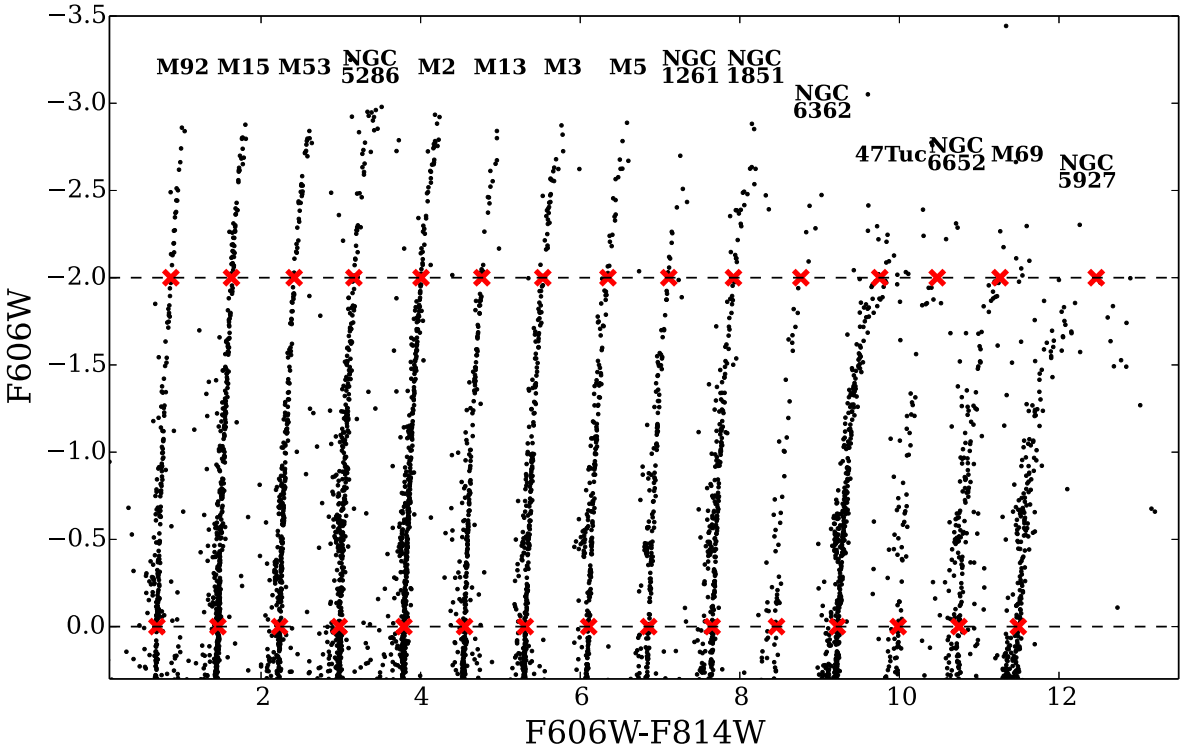

Figure A1. *F606W*, *F814W* photometry of Galactic GC RGBs, from the ACS Globular Cluster Survey (Sarajedini et al. 2007; Anderson et al. 2008). The cluster HBs were aligned, and the colours at two magnitudes ($M_V = 0$ and -2, shown as the horizontal dashed lines) were determined for each cluster; these values are shown as red crosses. The clusters are offset in the plot, and are ordered by metallicity (from Carretta et al. 2009a).

Table A2. PAndAS GC RGB slopes.

Cluster	[Fe/H]	RGB slope
PA06	-2.06 ± 0.10	-12.0482 ± 2.658
PA54	-1.84 ± 0.10	-11.173 ± 1.405
PA56	-1.73 ± 0.10	-10.811 ± 2.982
PA53	-1.64 ± 0.10	-10.526 ± 1.238
H10	-1.40 ± 0.10	-8.621 ± 0.813
H23	-1.12 ± 0.10	-7.353 ± 1.268

References: cluster [Fe/H] ratios are from the [Fe I/H] abundances in Table 6.

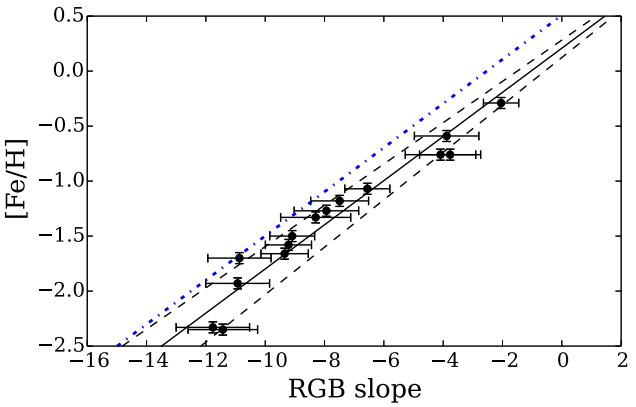

Figure A2. RGB slope versus [Fe/H] for the Galactic GCs. Slopes are determined using the points in Fig. A1; slope errors were estimated based on the uncertainties in these RGB colours.

which would affect where a cluster falls in the plot. The adopted [α/Fe] ratio is particularly important: the qualitative effects of [α/Fe] on the *F606W*, *F814W* RGB slope are illustrated in Fig. A3 using the Victoria–Regina isochrones from VandenBerg et al. (2014) and the colour transformations of Casagrande & VandenBerg (2014). Fig. 3(a) shows that at a given [Fe/H], clusters with [α/Fe] = 0 have steeper RGBs than clusters with [α/Fe] = +0.4; this offset is greater at higher metallicity. Furthermore, Fig. 3(b) illustrates that the slope difference can be mimicked by lowering [Fe/H] by 0.3 dex while maintaining [α/Fe] = +0.4 (note that in Fig. 3b the dotted isochrones have been shifted by 0.02 mag so that both the α-enhanced and α-normal isochrones can be seen). The blue dot–dashed line in Fig. A2 shows the effects of lowering [α/Fe] by 0.4 dex, which is approximated by lowering the [Fe/H] by 0.3 dex (also see Salaris et al. 1993).

The RGBs of the PAndAS clusters are shown in Fig. A4, while the RGB slopes and spectroscopic metallicities are shown in Fig. 4(b) and Table A2. The photometric uncertainties, sparseness of the CMDs, and difficulties in determining distance moduli (particularly for PA56) make the RGB slopes more uncertain for the PAndAS clusters, compared to the Galactic GCs. However, all PAndAS GCs agree with the MW RGB slope relation in Fig. A2 within their errors. This relationship illustrates that the spectroscopic metallicities are consistent with the observed RGB slopes in the *HST* CMDs. All of the clusters in Fig. 4(b) lie above the MW relation closer to the low [α/Fe] value, hinting at the possibility of low [α/Fe] ratios in the PAndAS targets.

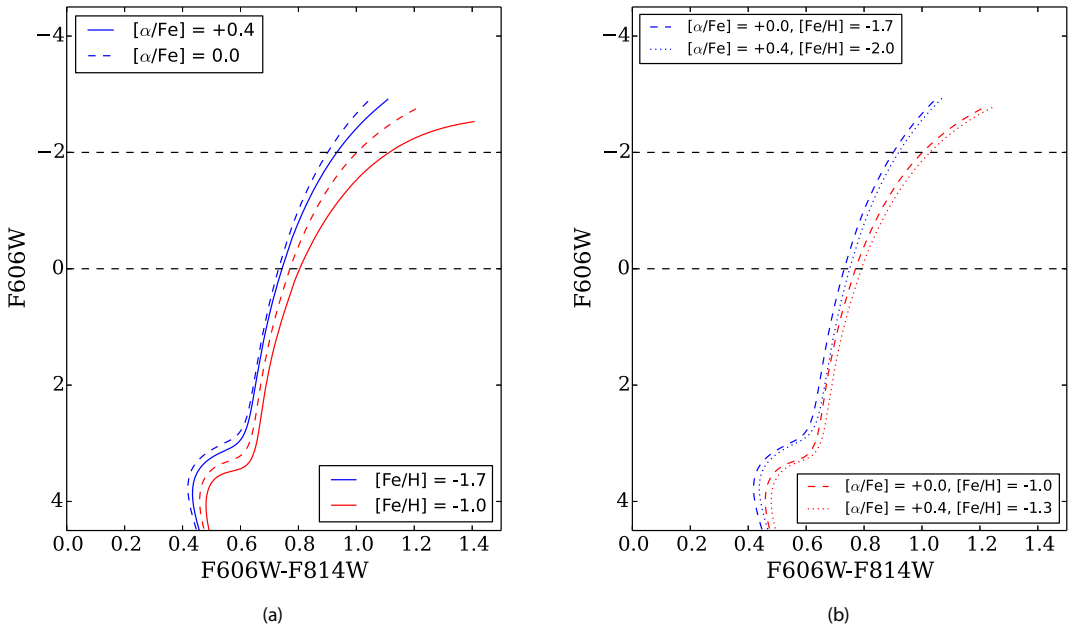

Figure A3. Victoria–Regina *F606W*, *F814W* isochrones from VandenBerg et al. (2014). Left: metal-poor ([Fe/H] $= -1.7$, in blue) and metal-rich ([Fe/H] $= -1.0$, in red) isochrones at two different values of [α/Fe]. The solid lines show [α/Fe] $= +0.4$, while the dashed lines show [α/Fe] $= 0.0$. Isochrones with low [α/Fe] have steeper RGB slopes at a fixed metallicity. Right: isochrones illustrating that the steeper slopes from [α/Fe] $= 0.0$ isochrones can be reproduced by lowering [Fe/H] by 0.3 dex while maintaining [α/Fe] $= +0.4$. The dashed lines show the same isochrones as in Fig. 3(a), while the dotted lines show isochrones with [α/Fe] $= +0.4$ and Δ[Fe/H] $= -0.3$ dex. The dotted isochrones are offset by $+0.02$ mag so that both isochrones can be seen. This shows that an [Fe/H] offset of -0.3 dex can be used in the RGB slope calibration to approximate the effects of lower [α/Fe].

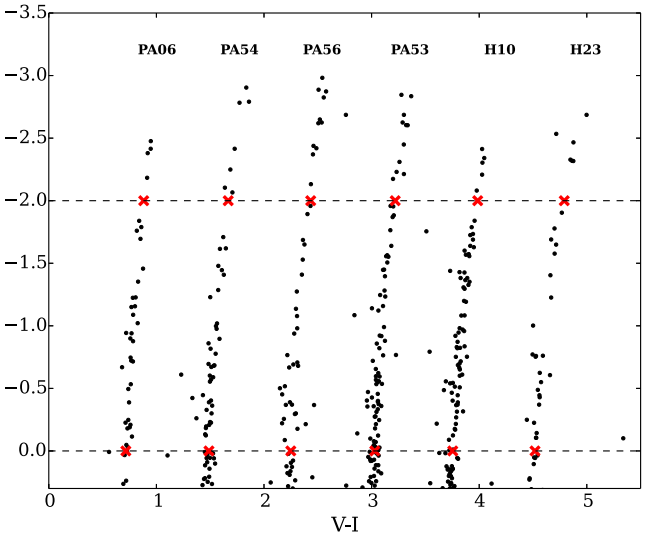

Figure A4. *F606W*, *F814W HST* photometry of PAndAS GCs, from Mackey et al. (in preparation). The cluster HBs were aligned, and the colours at two magnitudes ($M_V = 0$ and -2, shown as the horizontal dashed lines) were determined for each cluster; these values are shown as red crosses. The clusters are offset in the plot, and are ordered by metallicity.

SUPPORTING INFORMATION

Additional Supporting Information may be found in the online version of this article:

Table 3. The line list (http://mnras.oxfordjournals.org/lookup/suppl/doi:10.1093/mnras/stv020/-/DC1).

Please note: Oxford University Press is not responsible for the content or functionality of any supporting materials supplied by the authors. Any queries (other than missing material) should be directed to the corresponding author for the article.

This paper has been typeset from a TEX/LATEX file prepared by the author.